Theoretical and experimental analyses of the temperature responses of water-saturated rocks to changes in confining pressure

Xiaoqiu Yang[1], Weiren Lin[2], Hehua Xu[3], Osamu Tadai[4], and Xin Zeng[5]

[1]South China Sea Institute of Oceanology, Chinese Academy of Sciences
[2]Graduate School of Engineering, Kyoto University
[3]South China Sea Institute of Oceanology, Chinese Academy of Sciences, PRChina
[4]Marine Works Japan Ltd.
[5]Key Laboratory of Marginal Sea Geology

November 23, 2022

Abstract

The temperature response of water-saturated rocks to stress changes is critical for understanding thermal anomalies in the crust, because most porous rocks are saturated with groundwater. In this study, we establish a theoretical basis of the adiabatic pressure derivative of the temperature of water-saturated rocks under both undrained (βwet_U) and drained (βwet_D) conditions. The value of βwet_U is linearly correlated with Skempton's coefficient (B) and βwet_D increases nonlinearly as the pore water volume per unit volume of rock (ξ) increases. The theoretical calculations demonstrate that the thermal effects of pore water predominate in water-saturated rocks with medium to high porosity, especially under undrained conditions. In most cases, the temperature response of rocks with a porosity of > 0.05 under water-saturated and undrained conditions is greater than that under dry conditions. Experiments were also carried out on a water-saturated typical medium porosity sandstone (sample RJS, $= 0.102$) and on a compact limestone (sample L27, $= 0.003$) using an improved hydrostatic compression system. The experimental results confirm that the theoretical derivation is correct, and the calculated ranges of βwet_U and βwet_D are reliable for all 15 rocks. Consequently, this study increases our understanding of the thermal anomalies that occur after huge earthquakes, including the negative thermal anomalies, which are probably induced by co-seismic stress release, that were observed in the boreholes that penetrate seismic faults after the Chi-Chi Earthquake, the Wenchuan Earthquake, and the Tohoku Earthquake.

Theoretical and experimental analyses of the temperature responses of water-saturated rocks to changes in confining pressure

Xiaoqiu Yang[1, 2], Weiren Lin[3], Hehua Xu[1, 2], Osamu Tadai[4], Xin Zeng[1, 2]

[1]Key Laboratory of Ocean and Marginal Sea Geology, South China Sea Institute of Oceanology, Innovation Academy of South China Sea Ecology and Environmental Engineering, Chinese Academy of Sciences, Guangzhou 511458, China

[2]Southern Marine Science and Engineering Guangdong Laboratory (Guangzhou), Guangzhou 511458, China

[3]Graduate School of Engineering, Kyoto University, Kyoto 615-8540, Japan

[4]Marine Works Japan Ltd., Nankoku 783-8502, Japan

Corresponding author:

Xiaoqiu Yang (yxq2081@scsio.ac.cn), ORCID ID: 0000-0002-3113-8796

Key Points:

- Theory behind the temperature responses of water-saturated rocks to stress changes under undrained and drained conditions is established
- The thermal effects of pore water predominate in water-saturated rocks (porosity>0.05), especially under undrained conditions
- The temperature response of rocks (porosity>0.05) under water-saturated and undrained conditions is greater than that under dry conditions

Abstract

The temperature response of water-saturated rocks to stress changes is critical for understanding thermal anomalies in the crust, because most porous rocks are saturated with groundwater. In this study, we establish a theoretical basis of the adiabatic pressure derivative of the temperature of water-saturated rocks under both undrained (β_{wet_U}) and drained (β_{wet_D}) conditions. The value of β_{wet_U} is linearly correlated with Skempton's coefficient (B) and β_{wet_D} increases nonlinearly as the pore water volume per unit volume of rock (ξ) increases. The theoretical calculations demonstrate that the thermal effects of pore water predominate in water-saturated rocks with medium to high porosity, especially under undrained conditions. In most cases, the temperature response of rocks with a porosity of $\phi > 0.05$ under water-saturated and undrained conditions is greater than that under dry conditions. Experiments were also carried out on a water-saturated typical medium porosity sandstone (sample RJS, $\phi = 0.102$) and on a compact limestone (sample L27, $\phi = 0.003$) using an improved hydrostatic compression system. The experimental results confirm that the theoretical derivation is correct, and the calculated ranges of β_{wet_U} and β_{wet_D} are reliable for all 15 rocks. Consequently, this study increases our understanding of the thermal anomalies that occur after huge earthquakes, including the negative thermal anomalies, which are probably induced by co-seismic stress release, that were observed in the boreholes that penetrate seismic faults after the Chi-Chi Earthquake, the Wenchuan Earthquake, and the Tohoku Earthquake.

1. Introduction

The temperature response of water-saturated rocks to stress changes is crucial for understanding the thermal anomalies that have been observed in associated with various geological phenomena, such as earthquakes. *Milne* [1913] was the first to report slow temperature changes before large earthquakes. Recently, there have been increasing observations of thermal anomalies induced by seismic activity both terrestrially [*Wang and Zhu*, 1984; *Ma and Shan*, 2000; *Carreno et al.*, 2001; *Tronin et al.*, 2002; *Ouzounov and Freund*, 2004; *Wang et al.*, 2012; *Wang et al.*, 2013;

Chen et al., 2013, 2016, 2020; *Orihara et al.*, 2014] and above/below the seafloor [*Arai et al*., 2013; *Inazu et al.*, 2014].

With the exception of the positive thermal anomalies reported at fault slip interfaces in boreholes, negative thermal anomalies have been observed in the hanging wall and footwall blocks of faults after earthquakes, such as in the Chi-Chi Earthquake (1999, M_w 7.6) [*Kano et al.*, 2006; *Tanaka et al.*, 2006; *Tanaka et al.*, 2007], the Wenchuan Earthquake (2008, M_w 7.9) [*Li et al.*, 2013; *Li et al.*, 2015], and the Tohoku Earthquake (2011, M_w 9.0) [*Fulton et al.*, 2013]. Frictional heating during earthquake faulting is known to cause positive thermal anomalies [*Tanaka et al.*, 2006; *Fulton et al.*, 2013; *Li et al.*, 2015], but the causes of negative thermal anomalies have not been addressed in detail [*Yang et al*., 2020]. In fact, changes in co-seismic stress can contribute to temperature variations. There have been several theoretical and experimental studies on the thermoelastic response of rocks and the thermodynamics of minerals [*Waldbaum*, 1971; *Richter and Simmons*, 1974; *Wong and Brace*, 1979; *McTigue*, 1986; *Wong et al.*, 1987; *Wong et al.*, 1988; *Stixrude and Lithgow-Bertelloni*, 2005; *Ma et al.*, 2007; *Mosenfelder et al.*, 2007; *Chen et al.*, 2009; *Ma et al.*, 2012; *Chen et al.*, 2015]. A hydrostatic compression system has also been developed by the current authors [*Yang et al.*, 2018]. In the system, the rock specimen center can achieve adiabatic conditions during the first ~10 s after instant loading/unloading. The system was used to systematically test several representative sedimentary, igneous, and metamorphic rocks in the dry state [*Yang et al.*, 2017]. These results confirm that stress release/accumulation must cause a temperature decrease/increase. In recent years, *Chen et al*. [2016, 2019] observed the co-seismic bedrock temperature responses to the Lushan Earthquake (20 April 2013, M_s 7.0) and the Kangding Earthquake (22 November 2014, M_s 6.3) in Sichuan, China.

In the field, porous rocks are usually saturated with groundwater, especially at depth.

Compared with dry rocks, water-saturated rocks will exhibit different temperature responses to changes in co-seismic stress. The volumetric heat capacity of water ($(\rho c)_w$ is ~4.176 MJ/(m^3·K) [*Lide*, 2010]) is much higher than that of most dry rocks ($(\rho c)_{dry}$ is ~1.261–2.352 MJ/(m^3·K)) at room temperature [*Yang et al.*, 2017]. Consequently, it is anticipated that the adiabatic pressure derivative of the temperature of rocks under water-saturated conditions (β_{wet}) may be lower than that under dry conditions (β_{dry}) if there is no change in pore pressure before and after an earthquake. Nevertheless, the adiabatic pressure derivative of the temperature of water (β_w is ~17.67 mK/MPa) is an order of magnitude greater than that of dry rocks (β_{dry} is 1.5–6.2 mK/MPa) at ~20°C–23°C [*Yang et al.*, 2017]. Thus, the temperature response of pore water may be significant even if the pore pressure changes are small. In such cases, the co-seismic temperature response of water-saturated rocks under undrained conditions should be greater than that of dry rocks.

Since *Duhamel* [1837] and *Neumann* [1885], numerous studies on the thermoelasticity, poroelasticity, and the coupling on thermos-poroelasticity [*McTigue*, 1986, 1990] have been conducted, but the prior research has focused on either the temperature field influences on the stresses/strains [*Carlson*, 1973; *Wong and Brace*, 1979; *Nowacki*, 1986; *Wang et al.*, 1989; *Hetnarski and Eslami*, 2008] or the stress/strain influence on the temperature field of thermoelastic solids [*Duhamel*, 1837; *Neumann*, 1885; *Biot*, 1956; *Lessen*, 1956; *Boley and Weiner*, 1960] and pore pressure of porous rocks, respectively [*Biot*, 1941; *Geertsma*, 1957a]. *Geertsma* [1957b] and *Norris* [1992] discussed the analogous behavior of the temperature distribution in thermoelastic problems and the pore pressure distribution in a saturated porous medium. *Zimmerman* [2000] presented the dimensionless parameters that quantify the coupling strength between mechanical and hydraulic (or thermal) effects. The results show that 1) for fluid-saturated rocks, the mechanical deformation has a strong influence on the pore pressure; and 2) the thermoelastic coupling parameter is usually very small, so that the temperature field influences the stresses/strains, but the stresses/strains do not appreciably influence the temperature field.

After reviewing the theory of thermo-poroelasticity (provided in the Supporting Information), it can be found that a clear understanding of the temperature response of fluid-saturated porous rocks to changes in stress/strain has been lacking. Consequently, in this study, we analyze the theoretical basis of β in fluid-saturated rocks and carry out systematic experiments under undrained and drained conditions.

2. Theoretical Analyses

During most geological processes (plate motion, subduction), the pore fluid pressure (P_f) in the crust usually changes very slowly. However, rapid changes in pore pressure can occur during some sudden geological events, such as earthquakes [*Davis et al.*, 2000; *Manga et al.*, 2003; *Manga and Rowland*, 2009; *Davis et al.*, 2011; *Manga et al.*, 2012; *Davis et al.*, 2013; *Wang and Manga*, 2014; *Wang and Barbour*, 2017]. Therefore, this study analyzed and established the theoretical basis of the adiabatic temperature response of fluid-saturated rocks to stress changes. This was done specifically for water-saturated rocks (β_{wet}) subjected to loading and unloading of a confining pressure under undrained and drained conditions. The term undrained refers to the absence of change in the pore fluid mass ($dm_f = 0$) during sudden geological events; in contrast, the term drained refers to boundary conditions in which there are no pore fluid pressure changes ($dP_f = 0$), such as occur during slow geological processes. For a porous rock with a porosity ϕ, the factors (ρc), $(\rho c)_f$, and $(\rho c)_s$ are defined as the volumetric heat capacities of the fluid-saturated porous rock, the pore fluid and the solid grains, respectively. Consequently, the volumetric heat capacity of the fluid-saturated porous rock (ρc) can be expressed as

$$(\rho c) = (1 - \emptyset) \cdot (\rho c)_{\mathrm{s}} + \emptyset \cdot (\rho c)_{\mathrm{f}}. \quad (1)$$

For dry porous rocks and water-saturated porous rocks, the pores are filled with air and water, respectively. Thus, for dry porous rocks and water-saturated porous rocks, $(\rho c)_{\mathrm{f}}$ can be replaced with the volumetric heat capacity of air $(\rho c)_{\mathrm{a}}$, and the volumetric heat capacity of water $(\rho c)_{\mathrm{w}}$, respectively. Therefore, the volumetric heat capacity of dry and water-saturated porous rock, $(\rho c)_{\mathrm{dry}}$ and $(\rho c)_{\mathrm{wet}}$, respectively, can be expressed as

$$\begin{cases} (\rho c)_{\mathrm{dry}} = (1 - \emptyset) \cdot (\rho c)_{\mathrm{s}} + \emptyset \cdot (\rho c)_{\mathrm{a}} \\ (\rho c)_{\mathrm{wet}} = (1 - \emptyset) \cdot (\rho c)_{\mathrm{s}} + \emptyset \cdot (\rho c)_{\mathrm{w}} \end{cases}. \quad (2)$$

Generally, it is more convenient to measure the volumetric heat capacity of a dry rock than that of a water-saturated rock, e.g., with the transient plane source techniques [*Gustafsson*, 1991; *ISO*, 2008; *Lin et al.*, 2014; *Yang et al*., 2017]. If the porosity ϕ and volumetric heat capacity of dry rock $(\rho c)_{\mathrm{dry}}$ are measured, then $(\rho c)_{\mathrm{s}}$ and $(\rho c)_{\mathrm{wet}}$ can be calculated using the following equations:

$$\begin{cases} (\rho c)_{\mathrm{s}} = \left[(\rho c)_{\mathrm{dry}} - \emptyset \cdot (\rho c)_{\mathrm{a}}\right] / (1 - \emptyset) \\ (\rho c)_{\mathrm{wet}} = (\rho c)_{\mathrm{dry}} + \emptyset \cdot \left[(\rho c)_{\mathrm{w}} - (\rho c)_{\mathrm{a}}\right] \end{cases}. \quad (3)$$

If there is nothing within the pores, the porous rock is only a skeletal framework. Based on Equations (1) and (3), we can obtain the volumetric heat capacity of the skeletal framework of a porous rock $(\rho c)_{\mathrm{frm}}$

$$(\rho c)_{\mathrm{frm}} = (1 - \emptyset) \cdot (\rho c)_{\mathrm{s}} = (\rho c)_{\mathrm{dry}} - \emptyset \cdot (\rho c)_{\mathrm{a}}. \quad (4)$$

Under confining pressure P, $(\rho c)_{\mathrm{frm}}$ will increase due to the reduction in the rock's volume. Thus, $(\rho c)_{\mathrm{frm}} = (\rho c)_{\mathrm{frm0}}/(1\text{-}P/K_{\mathrm{P}})$, where $(\rho c)_{\mathrm{frm0}}$ is the volumetric heat capacity of the rock's skeletal framework at atmospheric pressure (P of ~ 0.1 MPa), K_{P} is the bulk modulus of the rock under confining pressure P. In this study, the confining pressure P is less than 50 MPa. The bulk modulus of crustal rocks K_{P} is up to ~5-50 GPa [*Goodman*, 1989; *Paterson and Wong*, 2005; *Yang et al.*, 2017]. Consequently, $(\rho c)_{\mathrm{frm}} \approx (\rho c)_{\mathrm{frm0}}$ since P/K_{P} tends to zero. Thus, in this study, the effect of confining pressure on the volumetric heat capacity of the rock is negligible.

2.1. The effective stress of fluid-saturated porous rock

In attempting to explain the time dependence of soil and sediment consolidation after loading, *Terzaghi* [1921] developed the notion of effective stress, which can be stated as $\sigma_{zz}^{\mathrm{eff}} = \sigma_{zz} - P_{\mathrm{f}}$. This means that the vertical effective stress $\sigma_{zz}^{\mathrm{eff}}$ is equal to the applied load σ_{zz} less the pore fluid pressure P_{f} that bears part of the load. It is deceptively simple [*Neuzil*, 2003]. *Nur and Byerlee* [1971] generalized *Terzaghi*'s effective stress law. They assumed that the strains can be expressed as linear combinations of the stresses within the elastic range of deformation of a porous solid and are linearly related to the pore pressure. They considered an isotropic aggregate of solid material with connected pores of arbitrary shapes and concentration, which they subjected it to a confining pressure P_{c} and a uniform pore fluid pressure P_{f}. Subsequently, they rigorously derived the exact expressions for effective stress from the basic principles.

$$\begin{cases} \sigma_{\mathrm{ij}}^{\mathrm{eff}} = \sigma_{\mathrm{ij}} - \alpha \cdot P_{\mathrm{f}} \cdot \delta_{\mathrm{ij}} \\ \alpha = 1 - (K/K_{\mathrm{s}}) \end{cases}, \quad (5)$$

where δ_{ij} is Kronecker's delta; α is the effective stress coefficient [*Gurevich*, 2004], which is the same with the Biot-Willis coefficient for an isotropic and homogeneous solid (monomineral) with the pore space characterized by a smooth boundary and filled with a homogeneous fluid [*Sahay*, 2013; *Müller and Sahay*, 2016; *Njiekak and Schmitt*, 2019]; K is the bulk modulus of the dry aggregate and K_{s} is the intrinsic bulk modulus of the solid grains. Additionally, K and K_{s} are demonstrated to represent the drained bulk modulus (i.e., $K = \Delta P_{\mathrm{c}}/(\Delta V/V)|_{\Delta P\mathrm{c}=0}$) and the unjacketed modulus (i.e., $K_s = \Delta P_c/(\Delta V/V)|_{Pc=Pf}$), respectively [*Wang*, 2000]. The volumetric strain $\Delta V/V$ is taken to be positive in contraction, and negative in expansion.

We define compression as positive. Therefore, the effective principal stresses are

$$\begin{cases} \sigma_{11}^{\mathrm{eff}} = \sigma_{11} - \alpha \cdot P_{\mathrm{f}} \\ \sigma_{22}^{\mathrm{eff}} = \sigma_{22} - \alpha \cdot P_{\mathrm{f}}. \\ \sigma_{33}^{\mathrm{eff}} = \sigma_{33} - \alpha \cdot P_{\mathrm{f}} \end{cases} \quad (6)$$

In a hydrostatic compression system, the principal stresses (σ_{11}, σ_{22} and σ_{33}) are the same to the confining pressure P_c. Thus, the effective pressure is

$$P^{\mathrm{eff}} = \left(\sigma_{11}^{\mathrm{eff}} + \sigma_{22}^{\mathrm{eff}} + \sigma_{33}^{\mathrm{eff}}\right)/3 = P_{\mathrm{c}} - \alpha \cdot P_{\mathrm{f}}. \quad (7)$$

Equations (5)–(7) accurately describe the behavior of fluid-saturated porous rocks, and has been demonstrated by *Nur and Byerlee* [1971] under laboratory conditions. *Nur and Byerlee*'s effective stress law is recognized and appears in pertinent textbooks and surveys on poroelasticity [*Bourbié et al.*, 1987; *Detournay and Cheng*, 1993; *Wang*, 2000; *Neuzil*, 2003; *Guéguen and Boutéca*, 2004; *Jaeger et al.*, 2007; *Cheng*, 2016; *Müller and Sahay*, 2019; *Meng et al.*, 2020].

If the changes in the effective pressure, confining pressure and pore pressure are defined as ΔP^{eff}, ΔP_c, and ΔP_f, respectively, then the change in the effective pressure can be expressed as

$$\Delta P^{\mathrm{eff}} = \Delta P_{\mathrm{c}} - \alpha \cdot \Delta P_{\mathrm{f}}. \quad (8)$$

This provides the relationship between the changes in the effective pressure (ΔP^{eff}), confining pressure (ΔP_c), and pore pressure (ΔP_f). Note that the porosity (ϕ) effect is not explicitly stated here, but is included in the effective bulk modulus of the dry aggregate K.

2.2. $\boldsymbol{\beta}_{\mathrm{wet\_U}}$ under Undrained Conditions

The term undrained refers to the boundary conditions in which there is no change in the pore fluid mass ($\mathrm{d}m_{\mathrm{f}}=0$). Thus, for porous rocks, Skempton's coefficient (B) is introduced. It is defined as the ratio of the pore fluid pressure change (ΔP_{f}) to the confining pressure change (ΔP_{c}) under undrained conditions, i.e., $B = (\Delta P_{\mathrm{f}}/\Delta P_{\mathrm{c}})|_{\mathrm{d}m_f=0}$ [*Skempton*, 1954; *Green and Wang*, 1986; *Wang*, 2000]. B is also referred to as the undrained pore pressure coefficient. Thus, the changes in pore pressure and effective pressure within the skeletal framework of the porous rock are expressed as

$$\begin{cases} \Delta P_{\mathrm{f}} = B \cdot \Delta P_{\mathrm{c}} \\ \Delta P^{\mathrm{eff}} = (1-\alpha \cdot B) \cdot \Delta P_{\mathrm{c}} \end{cases}. \quad (9)$$

There is a classical thermoelastic relationship between the temperature change (ΔT) and the confining pressure change (ΔP) [*Boley and Weiner*, 1960; *Wong et al.*, 1987; *Wong et al.*, 1988; *Turcotte and Schubert*, 2014; *Yang et al.*, 2017]

$$\begin{cases} \Delta T = \beta \cdot \Delta P \\ \beta = \dfrac{\alpha_{\mathrm{v}}}{\rho c_{\mathrm{p}}} \cdot T_0 \end{cases}, \quad (10)$$

where β is the adiabatic pressure derivative of the temperature $(\partial T/\partial P)_{\mathrm{s}}$ at thermodynamic temperature T_0, and α_{v} is the volumetric thermal expansion coefficient at T_0, which is three times the coefficient of linear thermal expansion (i.e., $\alpha_{\mathrm{v}} = 3\alpha_{\mathrm{l}}$) for isotropic materials. ρc_{p} is the heat capacity per volume at constant pressure. Consequently, at the moment the confining pressure instantaneously changes, the temperature changes in the pore fluid (ΔT_{f}) and the skeletal framework of the porous rock (ΔT_{frm}) can be obtained from the following equations:

$$\begin{cases} \Delta T_{\mathrm{frm}} = \beta_{\mathrm{frm}} \cdot \Delta P^{\mathrm{eff}} = (1-\alpha \cdot B) \cdot \beta_{\mathrm{frm}} \cdot \Delta P_{\mathrm{c}} \\ \Delta T_{\mathrm{f}} = \beta_{\mathrm{f}} \cdot \Delta P_{\mathrm{f}} = B \cdot \beta_{\mathrm{f}} \cdot \Delta P_{\mathrm{c}} \end{cases}, \quad (11)$$

where β_{frm} and β_{f} are defined as the adiabatic pressure derivatives of the temperature of the skeletal framework of the porous rock ($\beta_{\mathrm{frm}} = (\partial T_{\mathrm{frm}}/\partial P_{\mathrm{frm}})_{\mathrm{s}}$) and the pore fluid ($\beta_f = (\partial T_{\mathrm{f}}/\partial P_{\mathrm{f}})_{\mathrm{s}}$), respectively. Thus, the total heat energy change in the fluid-saturated porous rock per unit of bulk volume is

$$\Delta Q = \begin{cases} (\rho c)_{\mathrm{frm}} \cdot \Delta T_{\mathrm{frm}} + \emptyset \cdot (\rho c)_{\mathrm{f}} \cdot \Delta T_{\mathrm{f}} \\ \text{or} \\ [(1-\alpha \cdot B) \cdot (\rho c)_{\mathrm{frm}} \cdot \beta_{\mathrm{frm}} + \emptyset \cdot B \cdot (\rho c)_{\mathrm{f}} \cdot \beta_{\mathrm{f}}] \cdot \Delta P_{\mathrm{c}} \end{cases}. \quad (12)$$

Equation (11) demonstrates that there must be a temperature difference between the skeletal framework and the pore fluid, i.e., $\Delta T_{\mathrm{frm}} \neq \Delta T_{\mathrm{f}}$, at the moment at which the instantaneous change in the confining pressure occurs. In this study, we monitored the changes in the rock specimen temperature and the confining pressure using a data sampling interval of 1 s. For most of the porous rocks, the skeletal framework and the pore fluid (water) can reach thermal equilibrium by heat diffusion within 1 s of the instantaneous change in confining pressure since the sizes of the solid grains and the pores are limited. A detailed proof of the estimation of the characteristic distance using dimensional analysis and numerical simulation is provide in Section "Thermal equilibrium between the skeletal framework and the pore fluid" in Supporting Information. Consequently, Equations (1), (3), (4), and (12) can be combined to obtain the apparent temperature change of the fluid-saturated porous rock

$$\Delta T = \frac{\Delta Q}{(\rho c)} = \left\{ \frac{(1-\alpha \cdot B) \cdot [(\rho c)_{\mathrm{dry}} - \emptyset \cdot (\rho c)_{\mathrm{a}}] \cdot \beta_{\mathrm{frm}} + \emptyset \cdot B \cdot (\rho c)_{\mathrm{f}} \cdot \beta_{\mathrm{f}}}{(\rho c)_{\mathrm{dry}} + \emptyset \cdot [(\rho c)_{\mathrm{f}} - (\rho c)_{\mathrm{a}}]} \right\} \cdot \Delta P_{\mathrm{c}}. \quad (13)$$

Finally, β is calculated using the following equation:

$$\beta = \frac{\Delta T}{\Delta P_{\mathrm{c}}} = \frac{(1-\alpha \cdot B) \cdot [(\rho c)_{\mathrm{dry}} - \emptyset \cdot (\rho c)_{\mathrm{a}}] \cdot \beta_{\mathrm{frm}} + \emptyset \cdot B \cdot (\rho c)_{\mathrm{f}} \cdot \beta_{\mathrm{f}}}{(\rho c)_{\mathrm{dry}} + \emptyset \cdot [(\rho c)_{\mathrm{f}} - (\rho c)_{\mathrm{a}}]}. \quad (14)$$

The pores of dry porous rocks are filled with air, and thus, $(\rho c)_{\mathrm{f}}$ can be replaced with the volumetric heat capacity of air $(\rho c)_{\mathrm{a}}$. In the experiments on the temperature response to pressure changes in dry rocks [*Yang et al.*, 2017], the change in the pore-air pressure in dry rocks was ignored because its coefficient of compressibility is so high ($1/K_{\mathrm{a}} \rightarrow \infty$). In this case, Skempton's coefficient B for dry porous rocks tends toward zero ($B \rightarrow 0$) [*Wang*, 2000]. Consequently, the adiabatic pressure derivative of the temperature of dry porous rocks β_{dry} can be expressed as

$$\beta_{dry} = \frac{(1-\alpha\cdot B)\cdot[(\rho c)_{\mathrm{dry}}-\emptyset\cdot(\rho c)_{\mathrm{a}}]\cdot\beta_{\mathrm{frm}}+\emptyset\cdot B\cdot(\rho c)_{\mathrm{a}}\cdot\beta_{\mathrm{a}}}{(\rho c)_{\mathrm{dry}}+\emptyset\cdot[(\rho c)_{\mathrm{a}}-(\rho c)_{\mathrm{a}}]} = \frac{(\rho c)_{\mathrm{dry}}-\emptyset\cdot(\rho c)_{\mathrm{a}}}{(\rho c)_{\mathrm{dry}}}\cdot\beta_{\mathrm{frm}}. \quad (15)$$

In fact, under dry conditions, β_{dry} can be measured directly in laboratory experiments [*Yang et al.*, 2017]. Thus, β_{frm} can be calculated using the following equation:

$$\beta_{\mathrm{frm}} = \frac{(\rho c)_{\mathrm{dry}}}{(\rho c)_{\mathrm{dry}}-\emptyset\cdot(\rho c)_{\mathrm{a}}}\cdot\beta_{\mathrm{dry}}. \quad (16)$$

Thus, Equation (14) can be re-written as

$$\beta = \frac{\emptyset\cdot(\rho c)_{\mathrm{f}}\cdot\beta_{\mathrm{f}}-\alpha\cdot(\rho c)_{\mathrm{dry}}\cdot\beta_{\mathrm{dry}}}{(\rho c)_{\mathrm{dry}}+\emptyset\cdot[(\rho c)_{\mathrm{f}}-(\rho c)_{\mathrm{a}}]}\cdot B + \frac{(\rho c)_{\mathrm{dry}}\cdot\beta_{\mathrm{dry}}}{(\rho c)_{\mathrm{dry}}+\emptyset\cdot[(\rho c)_{\mathrm{f}}-(\rho c)_{\mathrm{a}}]}. \quad (17)$$

For water-saturated porous rocks, the pores are filled with water, therefore

$$\begin{cases}(\rho c)_{\mathrm{f}} = (\rho c)_{\mathrm{w}} \\ \quad \beta_{\mathrm{f}} = \beta_{\mathrm{w}}\end{cases}, \quad (18)$$

where $(\rho c)_{\mathrm{w}}$ and β_{w} are the heat capacity per unit volume and the adiabatic pressure derivative of the temperature of water, respectively. Based on Equations (17) and (18), the adiabatic pressure derivative of the temperature of water-saturated porous rocks under undrained conditions ($\beta_{\mathrm{wet\_U}}$) can be expressed as

$$\beta_{\mathrm{wet\_U}} = \frac{\emptyset\cdot(\rho c)_{\mathrm{w}}\cdot\beta_{\mathrm{w}}-\alpha\cdot(\rho c)_{\mathrm{dry}}\cdot\beta_{\mathrm{dry}}}{(\rho c)_{\mathrm{dry}}+\emptyset\cdot[(\rho c)_{\mathrm{w}}-(\rho c)_{\mathrm{a}}]}\cdot B + \frac{(\rho c)_{\mathrm{dry}}\cdot\beta_{\mathrm{dry}}}{(\rho c)_{\mathrm{dry}}+\emptyset\cdot[(\rho c)_{\mathrm{w}}-(\rho c)_{\mathrm{a}}]}. \quad (19)$$

Equation (19) shows that for porous rocks, $\beta_{\mathrm{wet\_U}}$ has a linear relationship with *B*, which depends on the physical properties of the porous rock, water, and air. These properties include the volumetric heat capacities $(\rho c)_{\mathrm{dry}}$, $(\rho c)_{\mathrm{w}}$, and $(\rho c)_{\mathrm{a}}$, the values of β_{dry} and β_{w}, and the porosity (ϕ).

2.3. $\boldsymbol{\beta}_{\mathbf{wet\_D}}$ under Drained Conditions

Relative to undrained conditions, the term drained refers to the boundary condition in which there is no change in the pore fluid pressure ($\Delta P_{\mathrm{f}} = 0$). Thus, in ideal drained conditions, for water-saturated porous rocks, the pore water pressure (P_{w}) will remain constant even if the confining pressure changes. In such a case, the value of ΔP_{w} is 0 (i.e., $\Delta P_{\mathrm{w}} = \Delta P_{\mathrm{f}} = 0$), and Equation (8) simplifies to

$$\Delta P^{\mathrm{eff}} = \Delta P_{\mathrm{c}}. \quad (20)$$

Therefore, we can express the temperature changes in the pore water (ΔT_{f}) and the skeletal framework of the porous rock (ΔT_{frm}) as

$$\begin{cases} \Delta T_{\mathrm{frm}} = \beta_{\mathrm{frm}} \cdot \Delta P^{\mathrm{eff}} = \beta_{\mathrm{frm}} \cdot \Delta P_{\mathrm{c}} \\ \Delta T_{\mathrm{w}} = \beta_{\mathrm{w}} \cdot \Delta P_{\mathrm{w}} = 0 \end{cases}. \quad (21)$$

Thus, the total heat energy change of the water-saturated porous rock per unit of bulk volume is

$$\Delta Q = (\rho c)_{\mathrm{frm}} \cdot \beta_{\mathrm{frm}} \cdot \Delta P_{\mathrm{c}}. \quad (22)$$

To account for the macroscopic stress or pore pressure, *Biot* [1941] introduced the variation in water content ξ, which is defined as the variation in the pore water volume per unit volume of rock.

$$\begin{cases} \xi = \dfrac{\Delta P_{\mathrm{c}}}{H} + \dfrac{\Delta P_{\mathrm{w}}}{R} \\ \dfrac{1}{H} = \dfrac{1}{K} - \dfrac{1}{K_s} \\ \dfrac{1}{R} = \dfrac{1}{H} + \emptyset \cdot \left(\dfrac{1}{K_{\mathrm{w}}} - \dfrac{1}{K_s}\right) \end{cases}, \quad (23)$$

where K_W is the bulk modulus of the pore water; $1/H$ and $1/R$ are the poroelastic expansion coefficient and the specific storage coefficient at constant stress, respectively [*Rice and Cleary*, 1976; *Wang*, 2000; *Paterson and Wong*, 2005]. A positive value of ξ indicates the removal of water.

Under drained conditions, there is no change in the pore water pressure ($\Delta P_w = 0$). Hence, Equation (23) can be re-written as

$$\xi = \frac{1}{H} \cdot \Delta P_c = \left(\frac{1}{K} - \frac{1}{K_s}\right) \cdot \Delta P_c, \quad (24)$$

and the volumetric heat capacity of the water-saturated porous rock after loading/unloading under drained conditions can be expressed as

$$(\rho c) = (1 - \emptyset) \cdot (\rho c)_s + (\emptyset - \xi) \cdot (\rho c)_w. \quad (25)$$

Thus, the apparent temperature change of water-saturated rocks under drained conditions is

$$\Delta T = \frac{\Delta Q}{(\rho c)} = \frac{(\rho c)_{frm} \cdot \beta_{frm}}{(1-\emptyset) \cdot (\rho c)_s + (\emptyset - \xi) \cdot (\rho c)_w} \cdot \Delta P_c. \quad (26)$$

Note that Equation (26) is also based on the fact that thermal equilibrium is reached between the solid grains and the pore water within 1 s after the instantaneous change in the confining pressure. Therefore, by combining Equations (3), (4), (16), and (20), the apparent adiabatic pressure derivative of the temperature of water-saturated porous rocks under drained conditions (β_{wet_D}) can be expressed as

$$\begin{cases} \beta_{wet\_D} = \frac{\Delta T}{\Delta P_c} = \frac{(\rho c)_{dry} \cdot \beta_{dry}}{(\rho c)_{dry} + \emptyset \cdot [(\rho c)_w - (\rho c)_a] - \xi \cdot (\rho c)_w} \\ \xi = \frac{1}{H} \cdot \Delta P_c \end{cases}. \quad (27)$$

3. Calculated β_{wet_U} and β_{wet_D} of 15 Representative Rocks

In our previous work, we systematically measured not only the basic physical properties of 15 representative rocks, but also the adiabatic pressure derivatives of temperature of the 15 dry rocks (β_{dry}) and water (β_w) at room temperature (21°C–23°C) [*Yang et al.*, 2017]. The basic physical properties of the 15 rocks include the grain density (ρ_s), the dry density (ρ_{dry}), the porosity (ϕ), the volumetric heat capacity in the dry state $(\rho c)_{dry}$, and the bulk modulus (K) in the dry state at 24°C–29°C and ~0.1 MPa. At 25°C and 0.1 MPa, the volumetric heat capacities of water ($(\rho c)_w$) and air ($(\rho c)_a$) are 4.169 MJ/(m^3·K) [*Lide*, 2010] and 1.206×10^{-3} MJ/(m^3·K) [*Yang and Tao*, 2006], respectively.

Based on the above-determined basic physical properties of the 15 rocks, water, and air, the apparent adiabatic pressure derivatives of the temperature of the water-saturated porous rocks under undrained and drained conditions (β_{wet_U} and β_{wet_D}) using Equations (19) and (27), respectively, can be calculated if the effective stress coefficient α, Skempton's coefficient B and poroelastic expansion coefficient $1/H$ are known. We did not measure α, B or $1/H$ for each rock used in this study. Instead, we compiled 32 published laboratory poroelastic constants for compact and porous rocks (including granites, carbonates and sandstones) (Table 1). Figures 1a and 1b indicate that α and $1/H$ increase approximately linearly with porosity ϕ. Most of the experimental results of α and $1/H$ are centrally distributed within the range delimited by Equations (28) and (29), respectively.

$$\text{FL01:} \quad \alpha = (0.9794 \cdot \phi + 0.5507) \pm 0.15,\ R^2 = 0.50, \tag{28}$$

$$\text{FL02:} \quad 1/H = (0.4988 \cdot \phi + 0.0015) \pm 0.06,\ R^2 = 0.65, \tag{29}$$

where the unit of $1/H$ is GPa^{-1}; and R^2 is the coefficient of determination. Figure 1a also shows that α usually ranges from ϕ to 1 (i.e., $\phi \leqslant \alpha \leqslant 1$) [*Berryman*, 1992; *Wang*, 2000]. From Equation (23), we know that $1/H$ must be more than 0 since the drained bulk modulus K is always less than the unjacketed modulus K_s, i.e., $1/H = (1/K-1/K_s) \geqslant 0$. Table 2 lists the estimated ranges of α and $1/H$ for the 15 rocks obtained from Equations (28) and (29). Even though Skempton's coefficient B tends to decrease with porosity ϕ, they are not directly related (Figure 1c). However, the value of B must be between 0 and 1. In this study, the change in confining pressure ΔP_c is between 0 and 15 MPa during the loading/unloading processes, i.e., $0 \leqslant |\Delta P_c| \leqslant 15$ MPa (Table 3).

Consequently, the ranges of β_{wet_U} and β_{wet_D} for the 15 rocks can be calculated using Equations (19) and (27) since the ranges of α, B, $1/H$ and ΔP_c are limited. We list the results in Table 2, and show the calculated β_{wet_U} with given α and B in Figure 2.

4. Experimental Methods and Results

4.1. Rock Samples

To verify the above theoretical analysis of the temperature response of fluid-saturated porous rocks to changes in stress, we systematically measured the β_{wet} of a low porosity (ϕ = 0.003) limestone (sample L27) and a medium porosity (ϕ = 0.102) sandstone (sample RJS). Samples L27 and RJS are from the Longmenshan Fault Zone in Sichuan, China, and the Rajasthan, India, respectively. Limestone L27 and sandstone RJS represent a compact rock and a porous rock, respectively. The two rock samples were cut into cylindrical specimens. The diameter (D_r) and length (L) of the rock specimens are both 50 mm (Figures 3 and 4). Their basic properties were measured at 24°C–29°C and ~0.1 MPa [*Yang et al.*, 2017]. The measured properties are listed in Table 2.

4.2. Measurement System and Experimental Procedure

In this study, it was necessary to measure the values of β_{wet_U} and β_{wet_D}, which required improvements to the hydrostatic compression system used to measure the adiabatic pressure derivative of the temperature of dry rocks (β_{dry}) [*Yang et al.*, 2017]. The improved hydrostatic compression system (Figure S1) and experimental procedure are similar to that used to measure β_{dry}, except for the inner structures related to the sample assembly. Thus, in this section, only the inner structures of the sample assembly (Figures 3 and 4) are described. Detailed descriptions of the measurement system and experimental procedure are provided in the Supporting Information.

To monitor the temperature response of the rock specimen, a small hole was drilled in the cylindrical rock sample center to allow for the installation of a temperature sensor. In this study, the diameter (D_h) and depth (H) of the central hole were 2.80 mm and 26.00 mm, respectively (Figures 3 and 4). The apparatus setup shown in Figure 3 was adapted for undrained conditions by inserting a steel tube into the central hole with a 0.15 mm gap between the walls of the steel tube and the hole. In addition, the apparatus setup shown in Figure 4 was used for drained conditions because there is nothing in the central hole except for the miniature temperature sensor T01. In reality, the cavity in the center of the rock sample was not an infinite reservoir that would allow for the pore pressure to drop to zero under ideal drained conditions, nor it was small enough or well-sealed enough to perfectly simulate ideal undrained conditions during the rapid loading/unloading processes. Therefore, in the experiments conducted in this study, we were able to closely approach the undrained/drained conditions, but we could not achieve the ideal undrained/drained conditions. Thus, the experiments conducted in this study can be considered to have been carried out under quasi-undrained/quasi-drained conditions.

4.3. Experimental Data Analysis and Results

A set of loading/unloading tests was carried out on water-saturated sandstone RJS and water-saturated limestone L27 (Table 3). We denote these tests as RJS(W)-13, -14, and -15 under quasi-undrained conditions (Figure 5), RJS(W)-16, -17, and -18 (Figure 6) and L27(W)-01, -02, and -03 (Figure 7) under quasi-drained conditions. All experimental data are not only listed in Table S1 in Supporting Information, but also stored and provided in a data repository (http://doi.org/10.5281/zenodo.4242969). The temperature records demonstrate that the temperature response characteristics in the center of the rock specimens differed under quasi-undrained conditions (Figure 5) and quasi-drained (Figures 6 and 7) conditions. Consequently, in this section, the temperature responses during loading/unloading under quasi-undrained and quasi-drained conditions are analyzed in detail, respectively.

4.3.1. Under Quasi-Undrained Conditions

Taking test RJS(W)-13 as an example, during the period of temperature equilibration, the confining pressure in Vessel B was maintained at 3.39 MPa, and the system's temperature tended to equilibrate at 22.725°C (Table 3). When valve V03 was rapidly opened manually (i.e., *Time* = 0 s in Figure 5), the confining pressure in Vessel B dropped from 3.39 MPa to atmospheric pressure (~0.1 MPa) within 1–2 s. Simultaneously, the temperature in the rock specimen center and the oil dropped rapidly.

The reason for the temperature change in the rock sample center ($\Delta T01$) during unloading (Figure 5a1) is not entirely clear because the temperature change in oil ($\Delta T03$) was much larger during the same period. However, $\Delta T01$ is the actual change in the rock sample's temperature that is required. Therefore, only the changes in the temperature in the rock specimen center and the pressure in Vessel B are shown in Figure 5a2. This illustrates that the temperature in the rock specimen decreased sharply to the lowest peak (-76 mK) during the first 3 s after the rapid unloading, and then, it increased during 3–13 s. The temperature peak (-76 mK) was induced by the temperature response of the water around the steel tube to the instantaneous confining pressure drop because the β of the water (β_{w}: ~17.0–26.0 mK/MPa, Table 3) is much greater than the β of dry rocks (β_{dry}: ~1.5–6.2 mK/MPa) at room temperature [*Yang et al.*, 2017]. This is discussed further in Section 5.1.

During the next several seconds (13–20 s), the central temperature remained nearly constant, much like the temperature steps in dry rock experiments conducted in a previous study [*Yang et al.*, 2017]. This means that, during the first ~20 s after rapid unloading, the central temperature of the rock specimen was only induced by the pressure change, but evidently not affected by the oil temperature change. Then, the temperature decreased gradually again because the specimen's center was affected by heat conduction due to the temperature difference between the specimen and the oil after the rapid unloading (Figure 5a1). Similar characteristics of temperature response are exhibited in tests RJS(W)-14 and -15 (Figures 5b2 and 5c2).

Consequently, the temperature changes (ΔT) indicated by the temperature steps (t=13–20 s) from tests RJS(W)-13, -14, and -15 were obtained. Then, the values of β_{wet_Meas} for sample RJS were calculated from the values of $\Delta T/\Delta P$. The results show that the β_{wet_Meas} of sample RJS are ~4.61–6.68 mK/MPa under quasi-undrained conditions (Figure 5, Table 3). These experimental results are larger than the calculated results (3.78–5.37 mK/MPa) of the water-saturated Rajasthan sandstone (Figure 2k, Table 2). The comparison is discussed further in Section 5.3.

4.3.2. Under Quasi-Drained Conditions

Under quasi-drained conditions, there were no sharp temperature peaks in the specimen's center after rapid loading/unloading (Figures 6 and 7). The characteristics of the temperature responses differ from those under quasi-undrained conditions (Figure 5) but are similar to those of the dry rock experiments [*Yang et al.*, 2017].

Here, we also take test L27(W)-01 as an example. In this test, the system temperature tended to equilibrate at 23.442°C (Table 3) more than 4 hours after placing the specimen in Vessel B. During this period, the confining pressure in Vessel B was maintained at atmospheric pressure. In Figure 7a, at t = 0 s, valve V02 was rapidly opened manually and valve V03 was kept closed. The confining pressure in Vessel B increased to ~6.83 MPa within 1–2 s (Figure 7a). It is worth noting that the temperature in the hole center increased gradually during the first ~7 s after rapid loading, after which it remained nearly constant from t = 7 s to t = 18 s. Then, it increased again because of heat conduction from the oil (Figure 7a). Figures 7b and 7c show similar temperature responses during the rapid unloading using the same procedure and operation as those used in experiments conducted on dry rocks in our previous study [*Yang et al.*, 2017]. The temperature steps (t=7–18 s) reveal that the central temperature of sample L27 was only caused by the pressure change, but not influenced by the oil temperature change during the first ~18 s. Distinct temperature steps also occurred in tests L27(W)-02 and -03 (Figures 7b2 and 7c2) and tests RJS(W)-16, -17, and -18 (Figures 6a2, 6b2 and 6c2) after rapid loading/unloading.

Consequently, the β_{wet_Meas} values of the water-saturated limestone and Rajasthan sandstone under quasi-drained conditions were determined from the values of $\Delta T/\Delta P$ based on the temperature steps observed in tests L27(W)-01, -02, and -03 (t = 7–18 s) and tests RJS(W)-16, -17, and -18 (t = 8–19 s), respectively. The measured

β_{wet_Meas} values of samples L27 and RJS are 0.92–1.50 mK/MPa and 3.57–3.61 mK/MPa, respectively (Figures 6 and 7, Tables 2 and 3), which are less than the calculated β_{wet_D} values (L27: 1.52–1.55 mK/MPa; RJS: 3.78–3.91 mK/MPa). A detailed comparison between the measured and calculated results is presented in Section 5.3.

5. Discussion

5.1. Temperature Response Characteristics under Quasi-Undrained and Quasi-Drained Conditions

Figures 5 and 6 (under undrained and drained conditions, respectively) show significantly different temperature response characteristics for the water-saturated sandstone RJS(W) after rapid loading/unloading, especially during the first ~10 s. Sharp temperature peaks occurred in tests RJS(W)-13, -14, and -15 under quasi-undrained condition, but did not occur in tests RJS(W)-16, -17 and -18 under quasi-drained condition.

As described in Section 4.2, in order to as closely as possible simulate drained conditions, only the miniature temperature sensor T01 was placed in the central hole (Figure 4). In this case, in tests RJS(W)-16, -17, and -18, the central hole, which had with a diameter of 2.80 mm, could not be filled fully by the pore water from the pores in the area around the central hole after the rapid loading/unloading. Consequently, during the first few seconds after the instant loading/unloading, there was no obvious change in the pore pressure in the area around the central hole, and no temperature peaks were recorded (Figure 6). Of course, there must be a change in pore pressure throughout the rock sample except for in the area directly around the hole.

In tests RJS(W)-13, -14, and -15 (Figure 5), to achieve undrained conditions, a steel tube with temperature sensor T01 was inserted in the central hole in the rock specimen (Figure 3). Between the steel tube and the hole wall, there was a very small 0.15 mm gap, which was easier to fill fully with the pore water from the pores in the area around the hole after rapid loading. Then, the water in the gap underwent compression/decompression during the loading/unloading processes, resulting in an instantaneous increase in temperature. This is the reason for the sharp temperature peaks during the first 3–4 s after rapid loading/unloading in tests RJS(W)-13, -14, and -15 (Figure 5) since the β value of water (β_{w}) reaches 17.76 mK/MPa at ~21°C and 26.03 mK/MPa at ~31°C (Table 3), which is much higher than the β value of dry rock (β_{dry}: ~1.5–6.2 mK/MPa) [*Yang et al*., 2017].

5.2. Ranges of β_{wet} under Undrained and Drained Conditions

In Section 2, the adiabatic pressure derivatives of the temperature of the water-saturated porous rocks under both undrained (β_{wet_U}) and drained (β_{wet_D}) conditions were deduced. The quantitative equation for β_{wet_U} and β_{wet_D} were also derived based on the basic physical properties of dry rocks, water, and air, as shown in Equations (19) and (27). However, it is difficult to obtain the values of α and B in Equation (19) and $1/H$ in Equation (27) during actual geological processes, i.e., the actual values of β_{wet_U} and β_{wet_D} cannot be calculated. However, it is still useful for understanding the temperature responses in various geological phenomena that induce changes in stress. Therefore, in this section, the ranges of β_{wet_U} and β_{wet_D} for all 15 rock samples are analyzed based on Equations (19) and (27). In addition, the basic physical properties of the rock samples (Table 2), water, and air are described in Section 3.

For undrained conditions, Figure 2 shows that β_{wet_U} decreases with B when $\phi < 0.05$, but increases with B when $\phi > 0.05$. This implies that β_{wet_U} will reach a maximum/minimum when B is 0 or 1. Therefore, according to Equation (19), the range of $\beta_{\mathrm{wet\_U}}$ can be obtained from the following equations.

If $\phi < 0.05$,

$$\frac{\emptyset\cdot(\rho c)_{\mathrm{w}}\cdot\beta_{\mathrm{w}}+(1-\alpha)\cdot(\rho c)_{\mathrm{dry}}\cdot\beta_{\mathrm{dry}}}{(\rho c)_{\mathrm{dry}}+\emptyset\cdot[(\rho c)_{\mathrm{w}}-(\rho c)_{\mathrm{a}}]} \le \beta_{\mathrm{wet\_U}} \le \frac{(\rho c)_{\mathrm{dry}}\cdot\beta_{\mathrm{dry}}}{(\rho c)_{\mathrm{dry}}+\emptyset\cdot[(\rho c)_{\mathrm{w}}-(\rho c)_{\mathrm{a}}]}, \quad (30)$$

and if $\phi > 0.05$,

$$\frac{(\rho c)_{\mathrm{dry}}\cdot\beta_{\mathrm{dry}}}{(\rho c)_{\mathrm{dry}}+\emptyset\cdot[(\rho c)_{\mathrm{w}}-(\rho c)_{\mathrm{a}}]} \le \beta_{\mathrm{wet\_U}} \le \frac{\emptyset\cdot(\rho c)_{\mathrm{w}}\cdot\beta_{\mathrm{w}}+(1-\alpha)\cdot(\rho c)_{\mathrm{dry}}\cdot\beta_{\mathrm{dry}}}{(\rho c)_{\mathrm{dry}}+\emptyset\cdot[(\rho c)_{\mathrm{w}}-(\rho c)_{\mathrm{a}}]}. \quad (31)$$

For drained conditions, Equation (27) illustrates that $\beta_{\mathrm{wet\_D}}$ decreases nonlinearly with increasing water content ξ (i.e., $\Delta P_{\mathrm{c}}/H$). During the drained loading process, the water content decreases with increasing confining pressure (i.e., $\Delta P_{\mathrm{c}} > 0$). Thus, the range of $\beta_{\mathrm{wet\_D}}$ can be obtained from the following equation:

$$\frac{(\rho c)_{dry}\cdot\beta_{dry}}{(\rho c)_{dry}+\emptyset\cdot[(\rho c)_{w}-(\rho c)_{a}]} \le \beta_{\mathrm{wet}\_D} \le \frac{(\rho c)_{\mathrm{dry}}\cdot\beta_{\mathrm{dry}}}{(\rho c)_{\mathrm{dry}}+\emptyset\cdot[(\rho c)_{\mathrm{w}}-(\rho c)_{\mathrm{a}}]-(\rho c)_{\mathrm{w}}\cdot\Delta P_{\mathrm{c}}/H}. \quad (32)$$

Conversely, during the drained unloading process, some of the water is absorbed into the rock pores because the pore space increases when the confining pressure decreases. The most extreme situation occurs when the confining pressure tends towards the atmospheric pressure (~0.1 MPa), resulting in the water content of the porous rocks reaching the maximum value. The volumetric heat capacity of the water-saturated rocks (the denominator term in Equation (27)) will be up to the maximum value. Hence, $\beta_{\mathrm{wet\_D}}$ will reach the minimum value. The porosities of all of the rocks were measured in our previous article [*Yang et al.*, 2017], implying that the left term in Equation (32) is also the lower limit of $\beta_{\mathrm{wet\_D}}$ during drained unloading.

From the above analysis, we obtained the following lower/upper limits for $\beta_{\mathrm{wet\_U}}$ and $\beta_{\mathrm{wet\_D}}$.

If $\phi < 0.05$,

$$\begin{cases} \beta_{\text{wet\_U\_Min}} = \frac{\emptyset \cdot (\rho c)_{\text{w}} \cdot \beta_{\text{w}} + (1-\alpha) \cdot (\rho c)_{\text{dry}} \cdot \beta_{\text{dry}}}{(\rho c)_{\text{dry}} + \emptyset \cdot [(\rho c)_{\text{w}} - (\rho c)_{\text{a}}]} \\ \beta_{\text{wet\_U\_Max}} = \beta_{\text{wet\_D\_Min}} = \frac{(\rho c)_{\text{dry}} \cdot \beta_{\text{dry}}}{(\rho c)_{\text{dry}} + \emptyset \cdot [(\rho c)_{\text{w}} - (\rho c)_{\text{a}}]} < \beta_{\text{dry}}, \\ \beta_{\text{wet\_D\_Max}} = \frac{(\rho c)_{\text{dry}} \cdot \beta_{\text{dry}}}{(\rho c)_{\text{dry}} + \emptyset \cdot [(\rho c)_{\text{w}} - (\rho c)_{\text{a}}] - (\rho c)_{\text{w}} \cdot \Delta P_{\text{c}} / H}, \Delta P_{\text{c}} > 0 \end{cases} \quad (33)$$

and if $\phi > 0.05$,

$$\begin{cases} \beta_{\text{wet\_U\_Max}} = \frac{\emptyset \cdot (\rho c)_{\text{w}} \cdot \beta_{\text{w}} + (1-\alpha) \cdot (\rho c)_{\text{dry}} \cdot \beta_{\text{dry}}}{(\rho c)_{\text{dry}} + \emptyset \cdot [(\rho c)_{\text{w}} - (\rho c)_{\text{a}}]} \\ \beta_{\text{wet\_U\_Min}} = \beta_{\text{wet\_D\_Min}} = \frac{(\rho c)_{\text{dry}} \cdot \beta_{\text{dry}}}{(\rho c)_{\text{dry}} + \emptyset \cdot [(\rho c)_{\text{w}} - (\rho c)_{\text{a}}]} \\ \beta_{\text{wet\_D\_Max}} = \frac{(\rho c)_{\text{dry}} \cdot \beta_{\text{dry}}}{(\rho c)_{\text{dry}} + \emptyset \cdot [(\rho c)_{\text{w}} - (\rho c)_{\text{a}}] - (\rho c)_{\text{w}} \cdot \Delta P_{\text{c}} / H}, \Delta P_{\text{c}} > 0 \end{cases} . \quad (34)$$

In fact, in Section 3, we calculated the lower and upper limits of β_{wet} for all of the 15 porous rocks used in this study (Table 2). Figure 8 illustrates the calculated ranges of β_{wet} under both undrained and drained conditions. Both of the calculated results and Equations (33) and (34) show that 1) when the porosity is within 0.05, the upper limit of $\beta_{\text{wet\_U}}$ equates to the lower limit of $\beta_{\text{wet\_D}}$, and both of them are less than β_{dry} (Figure 8a); and 2) when the porosity exceeds 0.05, the lower limits of $\beta_{\text{wet\_U}}$ and $\beta_{\text{wet\_D}}$ are the same, which indicate that there is no change in pore-water pressure (i.e., $B = 0$) under undrained conditions, and no change in the pore-water content (i.e., $\xi = 0$) under drained conditions. In addition, the upper limits of $\beta_{\text{wet\_U}}$ and $\beta_{\text{wet\_D}}$ indicate that the pore pressure change reaches a maximum, which equates to the change in confining pressure (i.e., $B = 1$), under undrained conditions, while part of the pore water has drained from the rock pores (i.e., $\xi = \Delta P_{\text{c}}/H$) under the drained conditions (Figure 8b). Figure 8 also clearly shows the following. 1) The range of $\beta_{\text{wet\_U}}$ contains the range of $\beta_{\text{wet\_D}}$, which is very narrow. This indicates that in most cases, it is sufficient only to analyze the lower and upper limits of β_{wet} under undrained conditions because most geological processes occur in between the undrained and drained conditions. 2) The range of β_{wet_U} becomes wider with the increase of porosity, especially when the porosity is greater than 0.05 (i.e., $\phi > 0.05$) (Figure 8b).

Also, the experimental results show that the values of B are typically between 0.5 and 1.0 for water-saturated rocks [*Wang*, 2000]; can be greater, e.g., 0.87–0.95 range for the Berea sandstone ($\phi \approx 0.20$), when the confining pressure is 40–60 MPa [*Green and Wang*, 1986]; can reach 0.97–0.99 for natural sandstone ($\phi \approx 0.15$) when the differential pressure is about 1 MPa [*Berge et al.*, 1993]; and can approach 1.0 for water-saturated soil [*Wang*, 2000]. In this study, the minimum values of β_{wet_U} for all of the 15 rocks were estimated when $B = 0.5$ using the same method as in Section 3. The results of $\beta_{wet\_U\_Min}(B{=}0.5)$ are shown in Figure 8 and are reported in Table 2. This indicates the following. 1) The values of β_{wet_U} will have a narrower range because B is typically in the 0.5–1.0 range under natural conditions, rather than 0–1. 2) When $B = 0.5$ and porosity is $\phi > 0.05$, the minimum values of β_{wet_U} are slightly lower than the β of dry rocks (β_{dry}), but they are very close to β_{dry} (Figure 8b). In other words, in most cases, the temperature response of rocks with a porosity of $\phi > 0.05$ under water-saturated and undrained conditions is greater than that under dry conditions. This is much more conducive to and important for understanding temperature response characteristics in nature, for example, the temperature anomalies in boreholes drilled through seismically active faults after the Chi-Chi Earthquake, the Wenchuan Earthquake, and the Tohoku Earthquake [*Kano et al.*, 2006; *Li et al.*, 2013; *Li et al.*, 2015; *Fulton et al.*, 2013].

5.3. Comparison between the Measured and Calculated β_{wet} Values

In Section 4, we systematically measured the β_{wet} of water-saturated limestone (L27, ϕ = 0.003) and sandstone (RJS, ϕ = 0.102). However, the measured β_{wet} of samples L27 and RJS were not entirely within the calculated ranges (Figure 8).

For the sandstone (RJS), the measured $\beta_{wet\_Meas(RJS)}$ under quasi-undrained conditions was 4.61–6.68 mK/MPa (Figure 5, Table 3), which is broadly larger than the calculated results under undrained conditions ($\beta_{wet\_U(RJS)}$ = 4.01–5.37 mK/MPa, even if B = 0.5–1.0) (Table 2). However, the measured $\beta_{wet\_Meas(RJS)}$ (3.57–3.61 mK/MPa) under quasi-drained conditions (Figure 6, Table 3) was lower than the calculated results for drained conditions ($\beta_{wet\_D(RJS)}$ = 3.78–3.91 mK/MPa) (Table 2). As was mentioned in Section 4.2, we drilled a hole in the center of the rock samples (D_h = 2.8 mm) and inserted a steel tube (D_{so} = 2.5 mm) containing temperature sensor T01 to as closely as possible approximate undrained conditions (Figure 3). To a large degree, the effective porosity of the rock samples, especially in the area around the steel tube, would significantly increase since there was a 0.15 mm gap between the walls of the steel tube and the hole. In the area around the steel tube (even if we cannot define the specific scope), if the effective porosity increases to 0.15 (denoted by ϕ'_{RJS} = 0.15), then we can estimate the ranges of $\beta_{wet\_U(RJS)}$ and $\beta_{wet\_D(RJS)}$ using Equations (19) and (27), respectively, using the same method (see Section 3). The estimated results are $\beta_{wet\_U(RJS)}$ = 4.34–6.25 mK/MPa when B ranges from 0.5 to 1.0, and $\beta_{wet\_D(RJS)}$ = 3.46–3.59 mK/MPa. In this case, the measured $\beta_{wet\_Meas(RJS)}$ is in good agreement with the theoretical estimates.

For the limestone (L27), the effective porosity also increased after drilling a 2.8 mm diameter hole. Using the same method, the ranges of $\beta_{wet\_U(L27)}$ and $\beta_{wet\_D(L27)}$ can be estimated if the effective porosity reached 0.01 (denoted by ϕ'_{L27} = 0.01) in the area around the hole. The range of $\beta_{wet\_U(L27)}$ was estimated to be 0.76–1.50 mK/MPa when B is 0–1. In addition, the range of $\beta_{wet\_D(L27)}$ was estimated to be 1.50–1.53 mK/MPa. The measured results for limestone L27 ($\beta_{wet\_Meas(L27)}$ = 0.92–1.50 mK/MPa, Figure 7 and Table 3) are in the range of $\beta_{wet\_U(L27)}$ (0.76–1.50 mK/MPa). This implies that the temperature response of the very low porosity rocks occurred under almost ideal undrained condition during the rapid loading/unloading processes, even the rock sample contained a central hole, which would be expected to result in drained conditions (Figure 4).

The above analysis indicates that the measured results are consistent with the calculated ranges for both the undrained and drained conditions. Consequently, both the theoretical analyses and the measurement results in this study are correct and reliable.

6. Conclusions

Determining the characteristics of the temperature responses of water-saturated rocks to stress changes is key for comprehending the temperature anomalies in the crust, particularly because most of the porous rocks in the upper crust are saturated with groundwater. Consequently, the adiabatic pressure derivative of the temperature of water-saturated rocks was established for both undrained (β_{wet_U}) and drained (β_{wet_D}) conditions. The theoretical derivation results show that β_{wet_U} is linearly correlated with Skempton's coefficient (B) and that β_{wet_D} increases nonlinearly with increasing pore water volume per unit volume of rock (ξ). Both β_{wet_U} and β_{wet_D} depend on the adiabatic pressure derivatives of the temperature of dry rocks and water, the volumetric heat capacities of dry rocks, water, and air, and rock's porosity. Based on the theoretical analysis, β_{wet_U} and β_{wet_D} were calculated for 15 rock samples. The calculated results indicate that the range of β_{wet_U} becomes wider with increasing porosity, especially when the porosity (ϕ) is greater than 0.05; while β_{wet_U} increases with increasing B when ϕ > 0.05, but decreases with increasing

B when $\phi < 0.05$. For each rock, the range of β_{wet_D} is very narrow and is within the range of β_{wet_U}. Thus, it is sufficient only to analyze the range of β_{wet} under undrained conditions since most geological processes occur between undrained and drained conditions.

Several experiments were carried out on water-saturated sandstone (RJS) and limestone (L27) using an improved hydrostatic compression system. The experiments show that under quasi-undrained conditions, the measured β_{wet_Meas} of sample RJS is 6.04–6.68 mK/MPa, which is broadly larger than the calculated $\beta_{wet\_U(RJS)}$ (4.01–5.37 mK/MPa) under undrained conditions, even when B was set to 0.5–1.0. However, under quasi-drained conditions, the measured $\beta_{wet\_Meas(RJS)}$ (3.57–3.61 mK/MPa) (Figure 6, Table 3) is lower than the calculated results under drained conditions ($\beta_{wet\_D(RJS)}$ = 3.78–3.91 mK/MPa). The measured $\beta_{wet\_Meas(RJS)}$ is in good agreement with the theoretical estimates after considering the increase in effective porosity caused by drilling a hole in the sample. The measured results for limestone L27, $\beta_{wet\_Meas(L27)}$ (0.92–1.50 mK/MPa), is in the range of the calculated $\beta_{wet\_U(L27)}$ (0.76–1.50 mK/MPa) after taking into account the increase in the effective porosity caused by drilling a hole in the sample. This implies that the temperature responses of the very low porosity rocks occurred under almost ideal undrained condition during loading/unloading processes. Overall, the measured results are consistent with the calculated results for both undrained and drained conditions, indicating that both the theoretical and experimental analyses are reliable.

Typically, B is in the 0.5–1.0 range for water-saturated rocks, rather than in the 0–1 range that occurs in natural conditions, implying that β_{wet_U} will be within a calculable and narrow range. In most cases, the temperature response of rocks with a porosity of $\phi > 0.05$ is greater under water-saturated and undrained conditions than that under dry conditions. This study improves our understanding of and preparation for co-seismic temperature responses, as there must be co-seismic stress changes in the future, such as the temperature anomalies observed in boreholes drilled through seismically active faults after the Chi-Chi, Wenchuan, and Tohoku earthquakes.

Data Availability Statement

Datasets for this research are available in *Yang et al*. [2020] and have been deposited in Zenodo (http://doi.org/10.5281/zenodo.4242969). The first dataset (Table S1) includes the temperature response of water-saturated porous Rajasthan sandstone (RJS) (Figures 5-6) and compact Longmenshan limestone (L27) (Figure 7) and to changes in confining pressure under drained/undrained conditions. The second dataset (Table S2) includes the thermal properties of rock-forming minerals and estimations of thermal characteristic time/distance. The third dataset includes the internal temperature evolution of the water-saturated sample within 1 s after instantaneous loading in models M-01 (Movie S1), M-02 (Movie S2) and M03 (Movie S3), in which the thermal properties of the solid grains are set to be that of gypsum, average values of the main rock-minerals and α-quartz, respectively. Meanwhile, all study data are included in the article and Supporting Information Appendix.

Acknowledgements

We thank Chi-Yuen Wang for helpful discussions, Zhigang Zhang for partial technical support to measure the temperature response of tap water at room temperature, and Takehiro Hirose and Huan Wang for providing the original photomicrographs of thin sections of Rajasthan sandstone from India and cataclasite and fault breccia from the Longmenshan Fault Zone, respectively. We really thank the two Reviewers, Associate Editor and Editor Douglas Schmitt for careful reading and constructive comments which help us to improve this manuscript. This work was supported by the Key Special Project for Introduced Talents Team of Southern

Marine Science and Engineering Guangdong Laboratory (Guangzhou) (GML2019ZD0104), the National Natural Science Foundation of China (41874099, 41474065 and 41376061) and the Instrument Developing Project of the Chinese Academy of Sciences (YZ201136). W. Lin acknowledges the supports of the Japan Society for the Promotion of Science (JSPS KAKENHI Grant Number JP16H04065).

References

Arai, K., et al. (2013), Tsunami-generated turbidity current of the 2011 Tohoku-Oki earthquake, Geology, 41(11), 1195-1198, doi:10.1130/G34777.1.

Berge, P. A., H. F. Wang, and B. P. Bonner (1993), Pore pressure buildup coefficient in synthetic and natural sandstones, International Journal of Rock Mechanics and Mining Sciences & Geomechanics Abstracts, 30(7), 1135-1141, doi:http://dx.doi.org/10.1016/0148-9062(93)90083-P.

Berryman, J. G. (1992), Exact effective-stress rules in rock mechanics, Physical Review A, 46(6), 3307-3311, doi:10.1103/PhysRevA.46.3307.

Biot, M. A. (1941), General Theory of Three ‐ Dimensional Consolidation, Journal of Applied Physics, 12(2), 155-164, doi:10.1063/1.1712886.

Biot, M. A. (1956), Thermoelasticity and Irreversible Thermodynamics, Journal of Applied Physics, 27(3), 240-253, doi:10.1063/1.1722351.

Boley, B. A., and J. H. Weiner (1960), Theory of thermal stresses, Wiley, New York.

Bourbié, T., O. Coussy, and B. Zinszer (1987), *Acoustics of porous media*, Editions Technip.

Carlson D.E. (1973) Linear Thermoelasticity. In: Truesdell C. (eds) Linear Theories of Elasticity and Thermoelasticity. Springer, Berlin, Heidelberg. https://doi.org/10.1007/978-3-662-39776-3_2

Carreno, E., R. Capote, A. Yague, J. Tordesillas, M. Lopez, J. Ardizone, A. Suarez, A. Lzquierdo, M. Tsige, and J. Martinez (2001), Observations of thermal anomaly associated to seismic activity from remote sensing, General Assembly of European Seismology Commission, Portugal, 265-269.

Cheng, A. H.-D. (2016), *Poroelasticity*, Springer International Publishing.

Chen, S., L. Liu, P. Liu, J. Ma, and G. Chen (2009), Theoretical and experimental study on relationship between stress-strain and temperature variation, Science in China Series D: Earth Sciences, 52(11), 1825-1834.

Chen, S., P. Liu, Y. Guo, L. Liu, and J. Ma (2015), An experiment on temperature variations in sandstone during biaxial loading, Physics and Chemistry of the Earth,

Parts A/B/C, 85–86, 3-8, doi:http://dx.doi.org/10.1016/j.pce.2014.10.006.
Chen, S., P. Liu, L. Liu, and J. Ma (2013), A phenomenon of ground temperature change prior to Lushan Earthquake observed in Kangding, Seismology and Geology, 35(3), 634-640.
Chen, S., P. Liu, L. Liu, and J. Ma (2016), Bedrock temperature as a potential method for monitoring change in crustal stress: Theory, in situ measurement, and a case history, Journal of Asian Earth Sciences, 123, 22-33, doi:http://dx.doi.org/10.1016/j.jseaes.2016.03.018.
Chen, S., P. Liu, Y. Guo, L. Liu, and J. Ma (2019), Co-Seismic Response of Bedrock Temperature to the Ms6.3 Kangding Earthquake on 22 November 2014 in Sichuan, China, Pure and Applied Geophysics, 176(1), 97-11, doi:10.1007/s00024-018-1933-7.
Chen, S., P. Liu, L. Chen, and Q. Liu (2020), Evidence from seismological observation for detecting dynamic change in crustal stress by bedrock temperature [in Chinese], *Chinese Science Bulletin*, *65*(22), 2395-2405, doi:10.1360/TB-2020-0089.
Coyner, K. B. (1984), Effects of stress, pore pressure, and pore fluids on bulk strain, velocity, and permeability of rocks, Ph.D. thesis, Massachusetts Institute of Technology, Cambridge.
De Simone, S., V. Vilarrasa, J. Carrera, A. Alcolea, and P. Meier (2013), Thermal coupling may control mechanical stability of geothermal reservoirs during cold water injection, Physics and Chemistry of the Earth, Parts A/B/C, 64, 117-126, doi:10.1016/j.pce.2013.01.001.
Demange, M. (2012), Mineralogy for petrologists : optics, chemistry, and occurrence of rock-forming minerals, edited, CRC Press, London, doi:10.1201/9780429355172.
Domenico, P. A., and F. W. Schwartz (1998), Physical and chemical hydrogeology, 2nd ed., John Wiley, New York.
Dong, H. (2008), Micro-CT imaging and pore network extraction, Ph.D. thesis, Imperial College London.
Detournay, E., and A. H. D. Cheng (1993), Fundamentals of Poroelasticity, in Comprehensive Rock Engineering: Principles, Practice and Projects, edited by J. A. Hudson, pp. 113-171, Pergamon Press, Oxford, UK, doi:https://doi.org/10.1016/B978-0-08-040615-2.50011-3.
Duhamel JMC (1837), Second mémoire sur les phénomènes thermo-mécaniques Second memoir on thermo-mechanical phenomena, Journal de l'Ecole Polytechnique, Tome 15, Cahier 25, pp 1–57.
Fulton, P. M., et al. (2013), Low Co-seismic Friction on the Tohoku-Oki Fault Determined from Temperature Measurements, Science, 342(6163), 1214-1217, doi:10.1126/science.1243641.

Geertsma J. (1957a), The effect of fluid Pressure decline on volumetric Changes of porous rocks，Petroleum Transactions, AIME, 210, 331-340.
Geertsma, J. (1957b), A remark on the analogy between thermoelasticity and the elasticity of saturated porous media, Journal of the Mechanics and Physics of Solids, 6(1), 13-16, doi: 10.1016/0022-5096(57)90042-X.
Ghassemi, A., and Q. Tao (2016), Thermo-poroelastic effects on reservoir seismicity and permeability change, Geothermics, 63, 210-224, doi: 10.1016/j.geothermics.2016.02.006.
Goodman, R. E. (1989), Introduction to Rock Mechanics, 2nd ed., JohnWiley & Sons, New York.
Green, D. H., and H. F. Wang (1986), Fluid pressure response to undrained compression in saturated sedimentary rock, Geophysics, 51(4), 948-956.
Gurevich, B. (2004), A simple derivation of the effective stress coefficient for seismic velocities in porous rocks, GEOPHYSICS, 69(2), 393-397, doi:10.1190/1.1707058.
Guéguen, Y., and M. Boutéca (2004), *Mechanics of Fluid-Saturated Rocks*, Academic Press.
Hart, D. J., and H. F. Wang (1995), Laboratory measurements of a complete set of poroelastic moduli for Berea sandstone and Indiana limestone, Journal of Geophysical Research: Solid Earth, 100(B9), 17741-17751, doi:10.1029/95JB01242.
Hashimoto, Y., K. Ujiie, A. Sakaguchi, and H. Tanaka (2007), Characteristics and implication of clay minerals in the northern and southern parts of the Chelung-pu fault, Taiwan, Tectonophysics, 443(3), 233-242.
Hetnarski, R. B., and M. R. Eslami (2008), Thermal Stresses—Advanced Theory and Applications (Solid Mechanics and Its Applications), Springer, Netherlands, doi:https://doi.org/10.1007/978-3-030-10436-8.
Inazu, D., Y. Ito, D. Saffer, and R. Hino (2014), An abrupt seafloor water-temperature increase in the epicentral region of the 2011 Tohoku earthquake, Japan Geoscience Union Meeting 2014.
Jaeger, J., N. G. Cook, and R. Zimmerman (2007), *Fundamentals of Rock Mechanics*, Blackwell.
Kano, Y., J. Mori, R. Fujio, H. Ito, T. Yanagidani, S. Nakao, and K.-F. Ma (2006), Heat signature on the Chelungpu fault associated with the 1999 Chi-Chi, Taiwan earthquake, Geophysical research letters, 33(14), L14306.
Lessen, M. (1956), Thermoelasticity and thermal shock, Journal of the Mechanics and Physics of Solids, 5(1), 57-61, doi:https://doi.org/10.1016/0022-5096(56)90007-2.
Li, H., H. Wang, Z. Xu, J. Si, J. Pei, T. Li, Y. Huang, S.-R. Song, L.-W. Kuo, and Z. Sun (2013), Characteristics of the fault-related rocks, fault zones and the principal

slip zone in the Wenchuan Earthquake Fault Scientific Drilling Project Hole-1 (WFSD-1), Tectonophysics, 584, 23-42.

Li, H., et al. (2015), Long-term temperature records following the Mw 7.9 Wenchuan (China) earthquake are consistent with low friction, Geology, 43(2), 163-166, doi:10.1130/g35515.1.

Lide, D. R. (2010), CRC handbook of chemistry and physics, 90th Edition (CD-ROM Version 2010), CRC press/Taylor and Francis, Boca Raton, Fla.

Ma, J., L. Liu, P. Liu, and S. Ma (2007), Thermal Precursory Pattern of Fault Unstable Slip: An Experimental Study of En Echelon Faults, Chinese Journal of Geophysics, 50(4), 995-1004.

Ma, J., and X. Shan (2000), An attempt to study fault activity using remote sensing technology-A case of the Mani earthquake, SEISMOLOGY AND GEOLOGY, 3, 000.

Ma, J., S. I. Sherman, and Y. Guo (2012), Identification of meta-instable stress state based on experimental study of evolution of the temperature field during stick-slip instability on a 5° bending fault, SCIENCE CHINA Earth Sciences, 55(6), 869-881, doi:10.1007/s11430-012-4423-2.

McTigue, D. F. (1986), Thermoelastic response of fluid-saturated porous rock, Journal of Geophysical Research: Solid Earth (1978–2012), 91(B9), 9533-9542.

McTigue, D. F. (1990), Flow to a heated borehole in porous, thermoelastic rock: Analysis, Water Resources Research, 26(8), 1763-1774, doi:10.1029/WR026i008p01763.

Meng, F., X. Li, P. Baud, and T. f. Wong (2020), Effective Stress Law for the Permeability and Pore Volume Change of Clayey Sandstones, *Journal of Geophysical Research: Solid Earth*, *125*(8), doi:10.1029/2020jb019765.

Milne, J. (1913), Earthquakes and other earth movements, London.

Mosenfelder, J. L., P. D. Asimow, and T. J. Ahrens (2007), Thermodynamic properties of Mg2SiO4 liquid at ultra-high pressures from shock measurements to 200 GPa on forsterite and wadsleyite, Journal of Geophysical Research: Solid Earth, 112(B6), B06208, doi:10.1029/2006JB004364.

Müller, T., and P. Sahay (2016), Biot coefficient is distinct from effective pressure coefficient, *GEOPHYSICS*, *81*, L1-L7, doi:10.1190/geo2015-0625.1.

Müller, T. M., and P. N. Sahay (2019), Elastic potential energy in linear poroelasticity, Geophysics, 84(4), W1-W20, doi:10.1190/geo2018-0216.1.

Neumann F (1885), Vorlesung über die Theorie des Elasticität der festen Körper und des Lichtäthers. Teubner, Leipzig (Meyer, Breslau).

Neuzil, C. E. (2003), Hydromechanical coupling in geologic processes, Hydrogeology Journal, 11(1), 41-83.

Njiekak, G., and D. R. Schmitt (2019), Effective Stress Coefficient for Seismic Velocities in Carbonate Rocks: Effects of Pore Characteristics and Fluid Types, *Pure and Applied Geophysics*, *176*(4), 1467-1485, doi:10.1007/s00024-018-2045-0.

Norris, A. (1992), On the correspondence between poroelasticity and thermoelasticity, Journal of Applied Physics, 71(3), 1138-1141, doi:10.1063/1.351278.

Nowacki, W. (1986), Thermoelasticity, 2nd ed., PWN-Polish Scientific Publishers, Warsaw, and Pergamon Press, Oxford, doi:10.1016/C2013-0-03247-1.

Nur, A., and J. D. Byerlee (1971), An exact effective stress law for elastic deformation of rock with fluids, Journal of Geophysical Research, 76(26), 6414-6419, doi:10.1029/JB076i026p06414.

Orihara, Y., M. Kamogawa, and T. Nagao (2014), Preseismic Changes of the Level and Temperature of Confined Groundwater related to the 2011 Tohoku Earthquake, Scientific reports, 4, doi:10.1038/srep06907.

Ouzounov, D., and F. Freund (2004), Mid-infrared emission prior to strong earthquakes analyzed by remote sensing data, Advances in Space Research, 33(3), 268-273.

Palciauskas, V. V., and P. A. Domenico (1989), Fluid pressures in deforming porous rocks, Water Resources Research, 25(2), 203-213, doi:doi:10.1029/WR025i002p00203.

Pan, Z. (1993), Crystallography and mineralogy, 3rd Edition [in Chinese], Geological Publishing House, Beijing.

Paterson, M. S., and T.-f. Wong (2005), Experimental Rock Deformation — The Brittle Field, 2nd ed., Springer-Verlag, Berlin.

Qin, Y., X. Yang, B. Wu, Z. Sun, and X. Shi (2013), High resolution temperature measurement technique for measuring marine heat flow, Sci. China Technol. Sci., 56(7), 1773-1778, doi:10.1007/s11431-013-5239-9.

Rice, J. R., and M. P. Cleary (1976), Some basic stress diffusion solutions for fluid-saturated elastic porous media with compressible constituents, Rev. Geophys. Space Phys, 14(2), 227-241, doi:10.1029/RG014i002p00227.

Richter, D., and G. Simmons (1974), Thermal expansion behavior of igneous rocks, paper presented at International Journal of Rock Mechanics and Mining Sciences & Geomechanics Abstracts, Elsevier.

Sahay, P. N. (2013), Biot constitutive relation and porosity perturbation equation, *GEOPHYSICS*, *78*(5), L57-L67, doi:10.1190/geo2012-0239.1.

Salimzadeh, S., A. Paluszny, H. M. Nick, and R. W. Zimmerman (2018), A three-dimensional coupled thermo-hydro-mechanical model for deformable fractured geothermal systems, Geothermics, 71, 212-224, doi:10.1016/j.geothermics.2017.09.012.

Schön, J. H. (2011), Physical properties of rocks: a workbook, Elsevier, Oxford.

Skempton, A. (1954), The pore-pressure coefficients A and B, Géotechnique, 4(4), 143-147.

Stixrude, L., and C. Lithgow-Bertelloni (2005), Thermodynamics of mantle minerals – I. Physical properties, Geophysical Journal International, 162(2), 610-632, doi:10.1111/j.1365-246X.2005.02642.x.

Tanaka, H., W. Chen, K. Kawabata, and N. Urata (2007), Thermal properties across the Chelungpu fault zone and evaluations of positive thermal anomaly on the slip zones: Are these residuals of heat from faulting?, Geophysical research letters, 34(1).

Tanaka, H., W. Chen, C. Wang, K. Ma, N. Urata, J. Mori, and M. Ando (2006), Frictional heat from faulting of the 1999 Chi‐Chi, Taiwan earthquake, Geophysical research letters, 33(16).

Teng, T., Y. Zhao, F. Gao, J. G. Wang, and W. Wang (2018), A fully coupled thermo-hydro-mechanical model for heat and gas transfer in thermal stimulation enhanced coal seam gas recovery, International Journal of Heat and Mass Transfer, 125, 866-875, doi:10.1016/j.ijheatmasstransfer.2018.04.112.

Terzaghi, K. (1923), Die Berechnung der Durchlässigkeitziffer des Tones aus dem Verlauf der hydrodymanischen Spannungserscheinungen [The computation of permeability of clays from the progress of hydrodynamic strain]. Akad der Wissenschaften in Wien, Sitzungsberichte, Mathematisch-naturwissenschaftliche Klasse, Part IIa, 132(3/4), pp 125–138

Tronin, A. A., M. Hayakawa, and O. A. Molchanov (2002), Thermal IR satellite data application for earthquake research in Japan and China, Journal of Geodynamics, 33(4), 519-534.

Turcotte, D., and G. Schubert (2014), Geodynamics, 3rd ed., Cambridge University Press, Cambridge, U. K.

Waldbaum, D. R. (1971), Temperature Changes associated with Adiabatic Decompression in Geological Processes, Nature, 232(5312), 545-547.

Wang, C., M. Manga, C. Wang, and C. Chin (2012), Transient change in groundwater temperature after earthquakes, Geology, 40, 119-122.

Wang, C. Y., L. P. Wang, M. Manga, C. H. Wang, and C. H. Chen (2013), Basin‐scale transport of heat and fluid induced by earthquakes, Geophysical Research Letters, 40(15), 3893-3897.

Wang, H. F. (2000), Theory of linear poroelasticity with applications to geomechanics and hydrogeology, edited, Princeton University Press, New Jersey.

Wang, H. F., B. P. Bonner, S. R. Carlson, B. J. Kowalls, and H. C. Heard (1989), Thermal stress cracking in granite, Journal of Geophysical Research, 94(B2), 1745-1758.

Wang, H., H. Li, J. Si, Z. Sun, and Y. Huang (2014), Internal structure of the Wenchuan earthquake fault zone, revealed by surface outcrop and WFSD-1

drilling core investigation, Tectonophysics, 619–620, 101-114, doi:10.1016/j.tecto.2013.08.029.
Wang, L., and C. Zhu (1984), Anomalous variations of ground temperature before the Tangsan and Haiheng earthquakes, J. Seismol. Res, 7(6), 649-656.
Wong, A. K., R. Jones, and J. G. Sparrow (1987), Thermoelastic constant or thermoelastic parameter?, Journal of Physics and chemistry of solids, 48(8), 749-753.
Wong, A. K., J. G. Sparrow, and S. A. Dunn (1988), On the revised theory of the thermoelastic effect, Journal of Physics and chemistry of solids, 49(4), 395-400, doi:http://dx.doi.org/10.1016/0022-3697(88)90099-6.
Wong, T.-f., and W. Brace (1979), Thermal expansion of rocks: some measurements at high pressure, Tectonophysics, 57(2), 95-117.
Xiao, Y., R. Zheng, and J. Deng (2017), Petrology introduction, 4th Edition [in Chinese], Geological Publishing House, Beijing.
Yang, S. M., and W. Q. Tao (2006), Heat transfer, 4th Edition [in Chinese], Higher Education Press, Beijing.
Yang, X., W. Lin, O. Tadai, X. Zeng, C. Yu, E.-C. Yeh, H. Li, and H. Wang (2017), Experimental and numerical investigation of the temperature response to stress changes of rocks, Journal of Geophysical Research: Solid Earth, 122(7), 5101-5117, doi:10.1002/2016JB013645.
Yang, X., W. Lin, O. Tadai, X. Zeng, X. Shi, and Z. Xu (2018), System for determining the adiabatic stress derivative of temperature for rock. US2018/0038812 A1.
Yang, X., W. Lin, E.-C. Yeh, H. Xu, and Z. Xu (2020), Analysis on the mechanisms of co-seismic temperature negative anomaly in fault zones [in Chinese], *Chinese Journal of Geophysics*, *63*(4), 1422-1430, doi:10.6038/cjg2020M0638.
Yang, X., W. Lin, O. Tadai, H. Xu, X. Zeng (2020), Temperature response of water-saturated compact Longmenshan limestone and porous Rajasthan sandstone to changes in confining pressure [Data set]. *Zenodo*. http://doi.org/10.5281/zenodo.4242969.
Zimmerman, R. W. (2000), Coupling in poroelasticity and thermoelasticity, International Journal of Rock Mechanics and Mining Sciences, 37(1), 79-87, doi: 10.1016/S1365-1609(99)00094-5.

Figure captions and Tables:

Figure 1. (a) Correlation between effective stress coefficient (a) and porosity (ϕ) where FL01 (the black line) is the linear fitting result for all 15 rocks, the pink dash line is $a = \phi$. The red and blue lines represent the maximum and minimum, respectively (similarly hereinafter). (b) Correlation

between poroelastic expansion coefficient $1/H$ and ϕ for all 15 rock samples where FL02 (the black line) is the linear fitting result. (c) The trend of Skempton's coefficient B with ϕ.

Figure 2. Graphical illustration of the calculated values of β_{wet_U} for 15 rock samples under undrained conditions. For each rock sample, the Skempton's coefficient B is in the 0–1 range; and the range of effective stress coefficient a is estimated from porosity ϕ based on Equation (28).

Figure 3. Apparatus setup for quasi-undrained conditions. (a) Diagrammatic sketch of rock specimen assembly. (b) The local structure around temperature sensor T01 (shown in green). (c, d, and e) Photographs of rock specimen assembly before and after being enveloped with rubber jacket and O-rings. HS, SS, RJ, HR, ST and TG are hard silicone (pink), soft silicone (dark gray), rubber jacket (orange), hard rubber (black), steel tube (light gray), and thermally conductive silicone grease (yellow), respectively. There is filled with water in the gap between rock specimen and steel tube. The temperature sensor size is 1.95 mm × 1.25 mm × 0.93 mm. The wire diameter is 0.2 mm.

Figure 4. Apparatus setup for quasi-drained conditions. (a) Diagrammatic sketch of rock specimen assembly. (b) The local structure around temperature sensor T01 (shown in green).

Figure 5. Changes in confining pressure in Vessel B (ΔP) and temperature (ΔT) during the unloading/loading processes of water-saturated Rajasthan sandstone (RJS(W)) under quasi-undrained conditions. T01 is in the rock specimen center, T02 is on the sample surface, and T03 is in oil in Vessel B. For each test, the background temperature T_0 (~22.5–24.0°C, Table 3) was removed, only temperature change was shown here. In these testes, the initial times represent the moments of rapid loading/unloading (similarly hereinafter).

Figure 6. Changes in confining pressure in Vessel B (ΔP) and temperature (ΔT) during the unloading/loading processes of water-saturated Rajasthan sandstone (RJS(W)) under quasi-drained conditions.

Figure 7. Changes in confining pressure in Vessel B (ΔP) and temperature (ΔT) during the loading/unloading processes of water-saturated Longmensan limestone (L27(W)) under quasi-drained conditions.

Figure 8. Calculated lower and upper limits of β_{wet} for all 15 rock samples when (a) Porosity (ϕ) is within 0.05 and (b) porosity (ϕ) ranges from 0.05 to 0.30. Red and pink circles represent the upper limits under undrained ($\beta_{wet\_U\_Max}$) and drained ($\beta_{wet\_D\_Max}$) conditions, respectively. Blue and green circles represent the lower limits in both undrained ($\beta_{wet\_U\_Min}$) and drained ($\beta_{wet\_D\_Min}$) conditions, respectively. Pink dots represent β_{wet_U} when B is 0.5 ($\beta_{wet\_U}(B=0.5)$). Blue triangles represent the lower limit under undrained conditions with Skempton's coefficient B = 0.5. Black circles represent the measured β of dry rocks (β_{dry}) [*Yang et al.*, 2017]. Orange stars denote measured values of β_{wet} in tests RJS(W)-13 to -18 and L27(W)-01 to -03.

Table 1. Collected laboratory data on poroelastic constants for compact and porous rocks [*Berryman*, 1992; *Wang*, 2000; *Paterson and Wong*, 2005]

No.		Rock	ϕ	K (GPa)	K_s (GPa)	B	α	$1/H$ (GPa^{-1})	*Pressure* (MPa)	Reference
1	Granite	Barre	0.027	15.0	53.0	0.62	0.72	0.04780	P_c-P_f ~ 10	[*Mesri et al.*, 1976]
2		Charcoal	0.020	35.0	45.0	0.55	0.22	0.00635		[*Rice and Cleary*, 1976]
3		Westerly	0.010	25.0	45.0	0.85	0.44	0.01778		[*Rice and Cleary*, 1976]
4		Westerly (red)	0.008	24.0	53.0		0.55	0.02280	P_c = 10	[*Coyner*, 1984; *Berryman*, 1992]
5		Westerly (red)	0.008	34.0	54.0		0.37	0.01089	P_c = 25	[*Coyner*, 1984; *Berryman*, 1992]
6		Chelmsford	0.011	17.0	55.5		0.69	0.04081	P_c = 25	[*Coyner*, 1984; *Berryman*, 1992]
7	Carbonate	Tennesse marble	0.020	40.0	50.0	0.51	0.20	0.00500		[*Rice and Cleary*, 1976]
8		Vermont marble	0.021	25.0	69.0	0.46	0.64	0.02551	P_c-P_f ~ 10	[*Mesri et al.*, 1976]
9		Salem limestone	0.126	13.0	38.0	0.32	0.66	0.05061	P_c-P_f ~ 10	[*Mesri et al.*, 1976]
10		Indiana limestone	0.130	21.2	72.6	0.46	0.71	0.03340	P_c-$\alpha \cdot P_f$ ~ 20-35	[*Hart and Wang*, 1995]
11		Tonnerre limestone	0.130	19.3	41.4	0.20	0.53	0.02766		[*Fabre and Gustkiewicz*, 1997]
12		Chauvigny limestone	0.165	16.3	52.6	0.20	0.69	0.04234	P_c ~ 100	[*Fabre and Gustkiewicz*, 1997]
13		Lavoux limestone	0.219	13.8	58.9	0.30	0.77	0.05549	P_c ~ 50	[*Fabre and Gustkiewicz*, 1997]
14		Lixhe chalk	0.428	3.8	42.5	0.35	0.91	0.23963		[*Fabre and Gustkiewicz*, 1997]
15		Bedford limestone	0.119	23.0	66.0		0.65	0.02833	P_c = 10	[*Coyner*, 1984; *Berryman*, 1992]
16		Bedford limestone	0.119	27.0	66.0		0.59	0.02189	P_c = 25	[*Coyner*, 1984; *Berryman*, 1992]
17	Sandstone	Boise	0.260	4.6	42.0	0.50	0.89	0.19358		[*Detournay and Cheng*, 1993]
18		Ohio	0.190	8.4	31.0	0.50	0.73	0.08679		[*Detournay and Cheng*, 1993]
19		Pecos	0.200	6.7	39.0	0.61	0.83	0.12361		[*Detournay and Cheng*, 1993]
20		Fontainebleau	0.060	30.9	35.2	0.25	0.12	0.00395	P_c = 90	[*Fabre and Gustkiewicz*, 1997]
21		Vosges (yellow)	0.170	17.4	42.5	0.46	0.59	0.03394		[*Fabre and Gustkiewicz*, 1997]
22		Vosges (red)	0.180	13.9	38.6	0.35	0.64	0.04604		[*Fabre and Gustkiewicz*, 1997]
23		Berea	0.190	8.0	36.0	0.62	0.78	0.09722		[*Rice and Cleary*, 1976]
24		Berea	0.190	6.6	28.9	0.75	0.77	0.11691	P_c-$\alpha \cdot P_f$ = 10	[*Hart and Wang*, 1995]
25		Berea	0.203	4.7	36.3	0.53	0.87	0.18522	P_c-P_f ~ 10	[*Mesri et al.*, 1976]

26	Berea	0.178	6.0	39.0		0.85	0.14103	Pc = 10	[*Coyner*, 1984; *Berryman*, 1992]
27	Berea	0.178	10.0	39.0		0.74	0.07436	Pc = 25	[*Coyner*, 1984; *Berryman*, 1992]
28	Navajo	0.118	13.0	34.0		0.62	0.04751	Pc = 10	[*Coyner*, 1984; *Berryman*, 1992]
29	Navajo	0.118	16.5	34.5		0.52	0.03162	Pc = 25	[*Coyner*, 1984; *Berryman*, 1992]
30	Weber	0.095	10.0	38.0		0.74	0.07368	Pc = 25	[*Coyner*, 1984; *Berryman*, 1992]
31	Weber	0.060	13.0	36.0	0.73	0.64	0.04915		[*Rice and Cleary*, 1976]
32	Ruhr	0.020	13.0	36.0	0.88	0.64	0.04915		[*Rice and Cleary*, 1976]

Note: ϕ, K and K_s are porosity, bulk modulus of dry aggregate and intrinsic bulk modulus of solid grains, respectively. B, a and $1/H$ are Skempton's coefficient, effective stress coefficient and poroelastic expansion coefficient, respectively.

Table 2. Physical Properties of the all 15 Rock Samples* and the estimated ranges of β_{wet_U} and β_{wet_D}

No.	Sample ID	Lithology or Material	Φ	$(\rho c)_{dry}$ (MJ/(m^3·K))	β_{dry} (mK/MPa)	Range of α	Range of β_{wet_U} when B = 0-1 (mK/MPa)	Range of β_{wet_U} when B = 0.5-1.0 (mK/MPa)	Range of 1/H (GPa^{-1})	Range of β_{wet_D} when $\lvert\Delta P_c\rvert \leq 15$ MPa (mK/MPa)	Note
1	L27	Limestone	0.003	2.287	1.53	0.403-0.703	0.54-1.52	1.03-1.52	0.000-0.063	1.52-1.55	From LMS Fault Zone
2	L35	Granite	0.005	2.352	3.16	0.406-0.706	1.08-3.13	2.10-3.13	0.000-0.064	3.13-3.18	From LMS Fault Zone
3	L24	Granodiorite	0.006	2.026	2.92	0.407-0.707	1.07-2.88	1.97-2.88	0.000-0.065	2.88-2.94	From LMS Fault Zone
4	L31	Lithic sandstone	0.012	2.158	3.58	0.412-0.712	1.39-3.50	2.45-3.50	0.000-0.067	3.50-3.57	From LMS Fault Zone
5	L25	Cataclasite	0.012	2.245	4.24	0.413-0.713	1.58-4.15	2.87-4.15	0.000-0.068	4.15-4.23	From LMS Fault Zone
6	L20	Sandstone	0.017	1.614	4.10	0.417-0.717	1.84-3.93	2.89-3.93	0.000-0.070	3.93-4.04	From LMS Fault Zone, black fault breccia
7	L23	Sandstone	0.019	1.869	4.35	0.420-0.720	1.90-4.18	3.04-4.18	0.000-0.071	4.17-4.27	From LMS Fault Zone, black fault breccia
8	L17	Sandstone	0.043	1.750	4.03	0.443-0.743	2.58-3.68	3.12-3.68	0.000-0.083	3.65-3.75	From LMS Fault Zone, black fault breccia
9	KBT	Basalt	0.076	1.967	2.69	0.475-0.775	2.32-3.66	2.64-3.66	0.000-0.099	2.32-2.38	From Karatsu, Saga Prefecture, Japan
10	L28	Siltstone	0.100	1.261	3.66	0.499-0.799	2.75-5.77	3.85-5.77	0.000-0.111	2.75-2.87	From LMS Fault Zone
11	RJS	Sandstone	0.102	1.737	4.71	0.500-0.800	3.78-5.37	4.01-5.37	0.000-0.112	3.78-3.91	From Rajasthan, India
12	C01	Siltstone	0.110	1.991	4.28	0.509-0.809	3.48-5.03	3.73-5.03	0.000-0.116	3.48-3.59	From TCDP Hole-A, Chelungpu Fault. The depth is 1105.43-1105.73 m
13	C02	Sandstone with bioturbation	0.122	2.192	4.81	0.520-0.820	3.90-5.21	3.97-5.21	0.002-0.122	3.90-4.02	From TCDP Hole-A, Chelungpu Fault. The depth is 484.75~484.93 m
14	BRS	Sandstone	0.200	1.528	5.86	0.579-0.879	3.79-7.78	5.21-7.78	0.041-0.161	3.79-3.96	From Berea, Ohio, USA
15	TTF	Welded tuff	0.300	1.471	6.15	0.694-0.994	3.32-9.14	5.73-9.14	0.091-0.211	3.32-3.49	From Tage, Tochigi Prefecture, Japan

* ϕ, $(\rho c)_{dry}$ and β_{dry} are the measured porosity, volumetric heat capacity and adiabatic pressure derivative of the temperature $(\partial T/\partial P)_s$ of the dry rock sample at room temperature [*Yang et al*., 2017].
Ranges of α and 1/H were estimated from porosity ϕ based on equations (28) and (29), respectively. Ranges of β_{wet_U} and β_{wet_D} are calculated according to equations (19) and (27), respectively.

Table 3. Key Experimental Records and Results of Water-Saturated Rock Samples and Tap Water during Loading/Unloading Processes[a]

No.	Sample ID	Test	T_0 (°C)	P_0 (MPa)	P_{End} (MPa)	ΔP (MPa)	ΔT (mK)	β_{wet_Meas} (mK/MPa)	Conditions
1	RJS(W)	-13	22.725	3.39	-0.04	-3.43	-22.93	6.68	Quasi-undrained
2	RJS(W)	-14	22.497	6.96	-0.04	-6.99	-42.20	6.04	Quasi-undrained
3	RJS(W)	-15	23.619	-0.07	9.32	9.39	43.30	4.61	Quasi-undrained
4	RJS(W)	-16	23.737	4.79	-0.01	-4.80	-17.15	3.57	Quasi-drained
5	RJS(W)	-17	23.369	9.78	-0.01	-9.79	-35.32	3.61	Quasi-drained
6	RJS(W)	-18	23.356	2.08	15.05	12.97	46.50	3.59	Quasi-drained
7	L27(W)	-01	23.442	0.00	6.83	6.83	10.30	1.50	Quasi-drained
8	L27(W)	-02	23.186	6.90	-0.04	-6.94	-6.38	0.92	Quasi-drained
9	L27(W)	-03	23.893	9.86	-0.03	-9.89	-9.37	0.95	Quasi-drained
10	WT[b]	-01	21.233	50.00	0.00	-50.00	-882.10	17.64	
11	WT[b]	-02	21.231	50.00	0.00	-50.00	-885.30	17.71	
12	WT[c]	-03	31.156	10.03	21.17	11.14	290.00	26.03	

[a] T_0 is the background temperature before loading/unloading. P_0 and P_{End} are the initial and end confining pressure in Vessel B during loading/unloading process, respectively. ΔP and ΔT are the changes in confining pressure in Vessel B and temperature in the center of rock specimen during loading/unloading process, respectively. β_{wet} is the measurement result of the adiabatic pressure derivative of temperature of water-saturated rock under undrained condition at T_0 for each test.

[b] The results were from two temperature loggers, #002 and #107, in a big pressure vessel filled with tap water during unloading process, at the Guangzhou Marine Geological Survey, China.

[c] The result was from the temperature logger, #095949, in a big pressure vessel filled with tap water during loading process, at the Hadal Science and Technology Research Center, Shanghai Ocean University, China.

Figure captions:

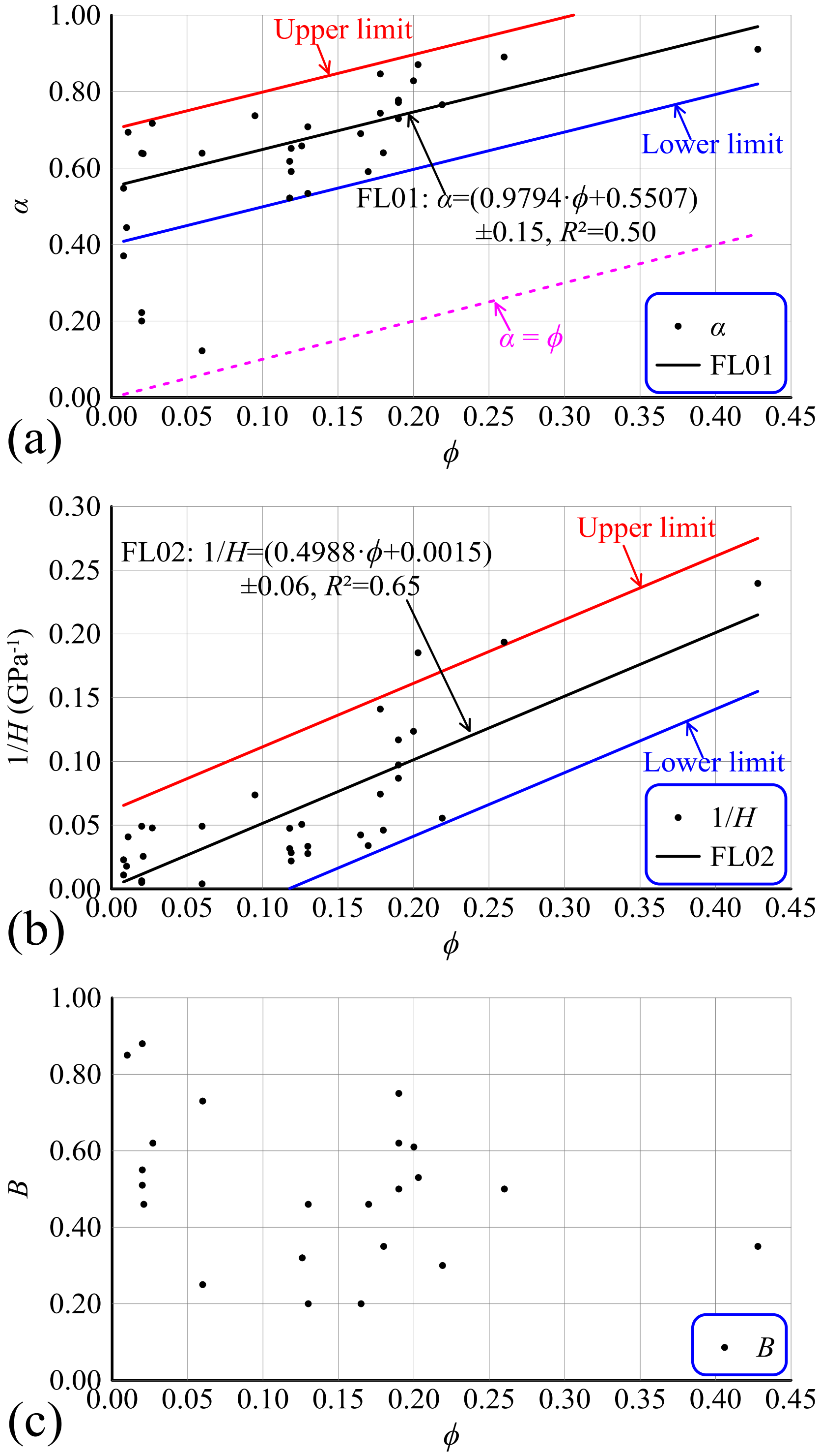

Figure 1. (a) Correlation between effective stress coefficient (a) and porosity (ϕ) where the black line (FL01) is the linear fitting curve for all 15 rock samples, the pink dash line is $a = \phi$. The red and blue lines represent the upper and lower limits, respectively (similarly hereinafter). (b) Correlation between poroelastic expansion coefficient $1/H$ and ϕ for all 15 rock samples where the black line (FL02) is the linear fitting curve. (c) The trend of Skempton's coefficient B with ϕ.

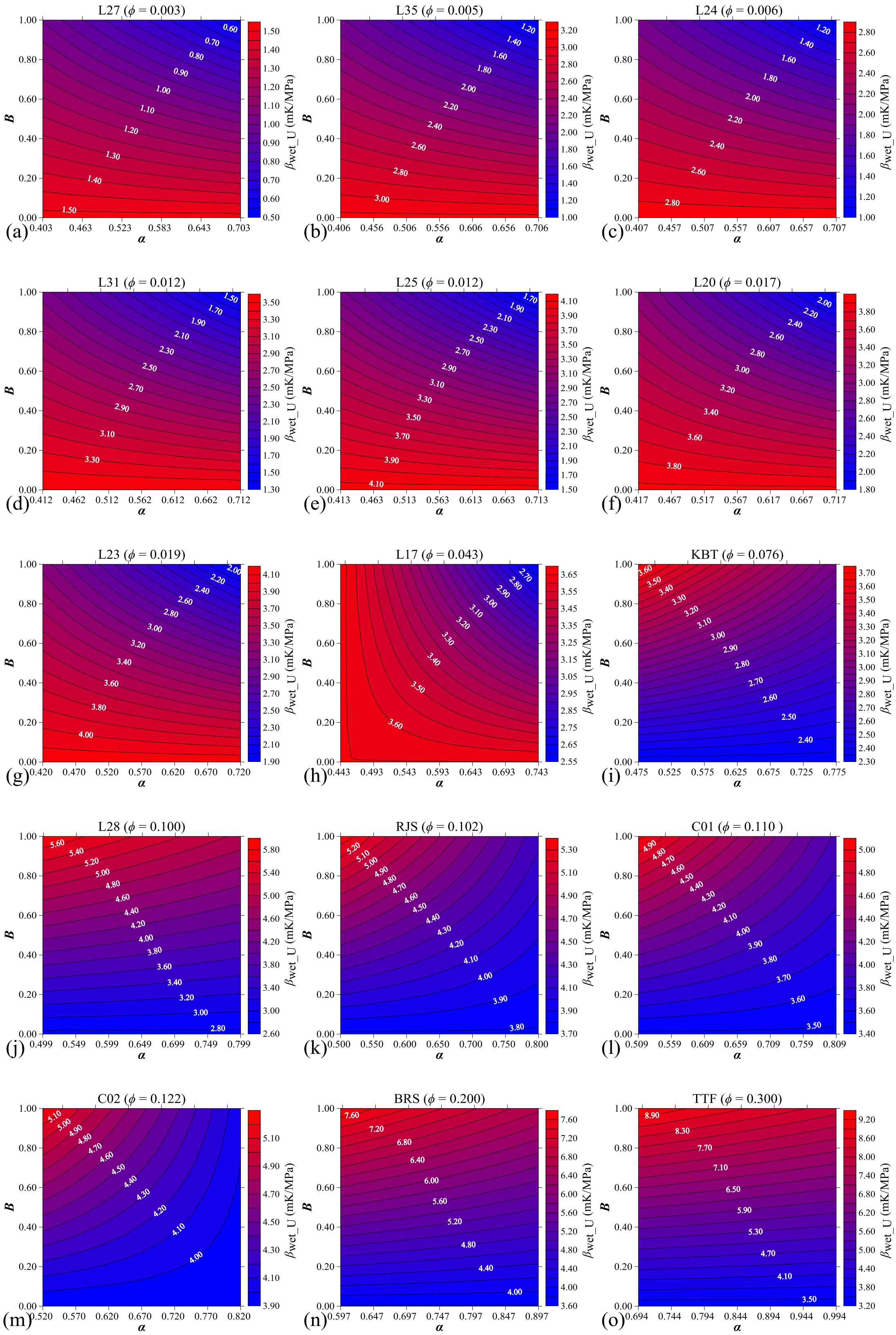

Figure 2. Graphical illustration of the calculated values of β_{wet_U} for 15 rock samples under undrained conditions. For each rock sample, the Skempton's coefficient B is in the 0–1 range; and the range of effective stress coefficient a is estimated from porosity ϕ based on equation (18).

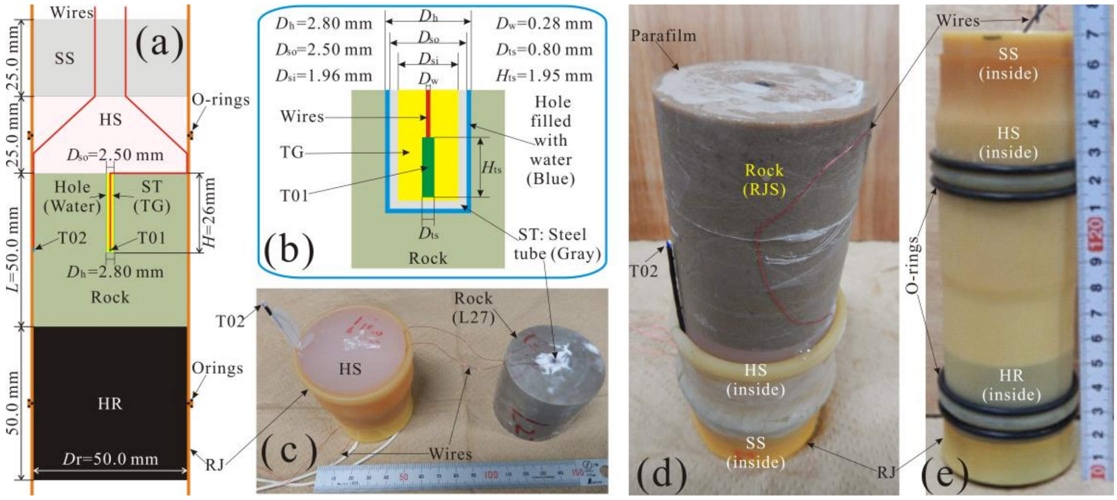

Figure 3. Apparatus setup for quasi-undrained conditions. (a) Schematic diagram of rock specimen assembly. (b) Local structure around temperature sensor T01 (shown in green). (c, d) Photographs of rock specimen assembly before being enveloped with rubber jacket and O-rings and (e) after being enveloped with rubber jacket and O-rings. HS is hard silicone (pink), SS is soft silicone (dark gray), RJ is rubber jacket (orange), HR is hard rubber (black), ST is steel tube (light gray) (water is placed in the gap between rock specimen and ST) and TG is thermally conductive silicone grease (yellow). The size of miniature temperature sensors is 1.95 mm × 1.25 mm × 0.93 mm and the diameter of the wires is 0.2 mm. The equivalent diameters of T01 and the two wires are 0.8 mm and 0.28 mm, respectively.

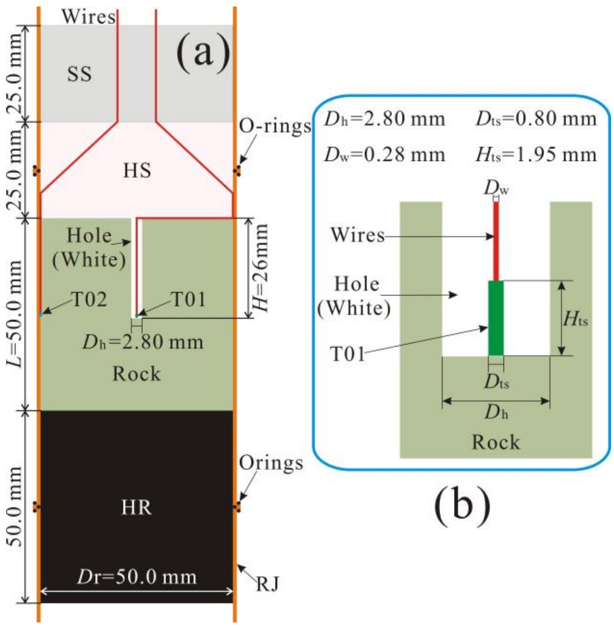

Figure 4. Apparatus setup for quasi-drained conditions. (a) Schematic diagram of rock specimen assembly. (b) Local structure around temperature sensor T01 (shown in green).

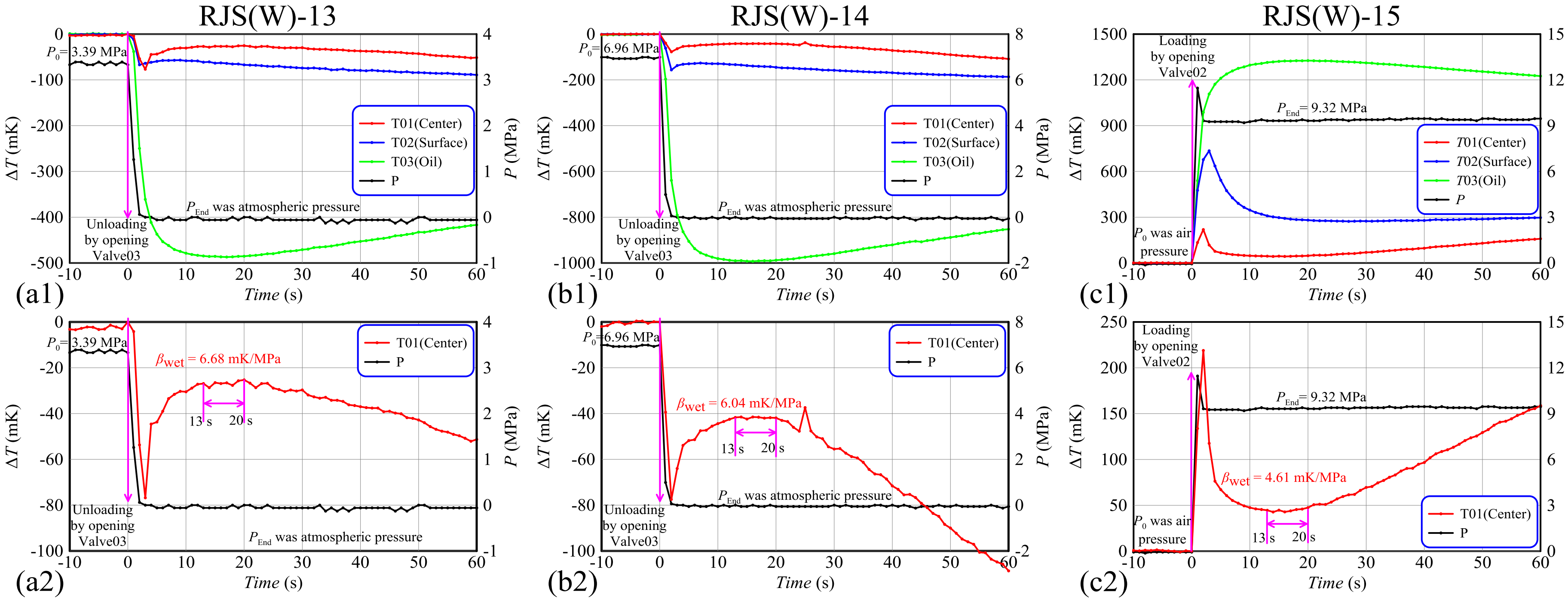

Figure 5. Changes of confining pressure (ΔP, in Vessel B) and temperature (ΔT) during the unloading/loading processes of water-saturated Rajasthan sandstone (RJS(W)) under quasi-undrained conditions. T01 is in the rock sample center, T02 is on the surface of sample, and T03 is in oil in Vessel B. For each test, the background temperature T_0 (~22.5–24.0°C, Table 3) was removed, only temperature change was shown here. In these testes, the points of rapid loading/unloading are set to be the initial times (similarly hereinafter).

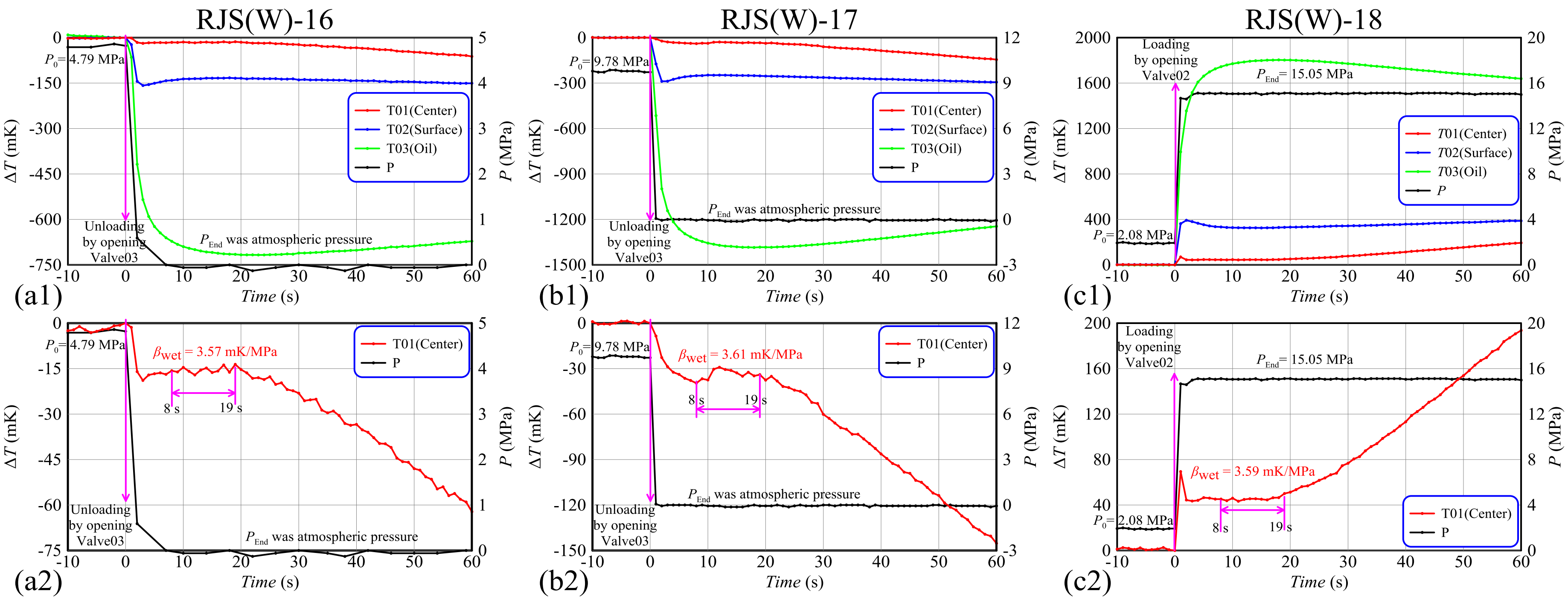

Figure 6. Changes of confining pressure (ΔP, in Vessel B) and temperature (ΔT) during the unloading/loading processes of water-saturated Rajasthan sandstone (RJS(W)) under quasi-drained conditions.

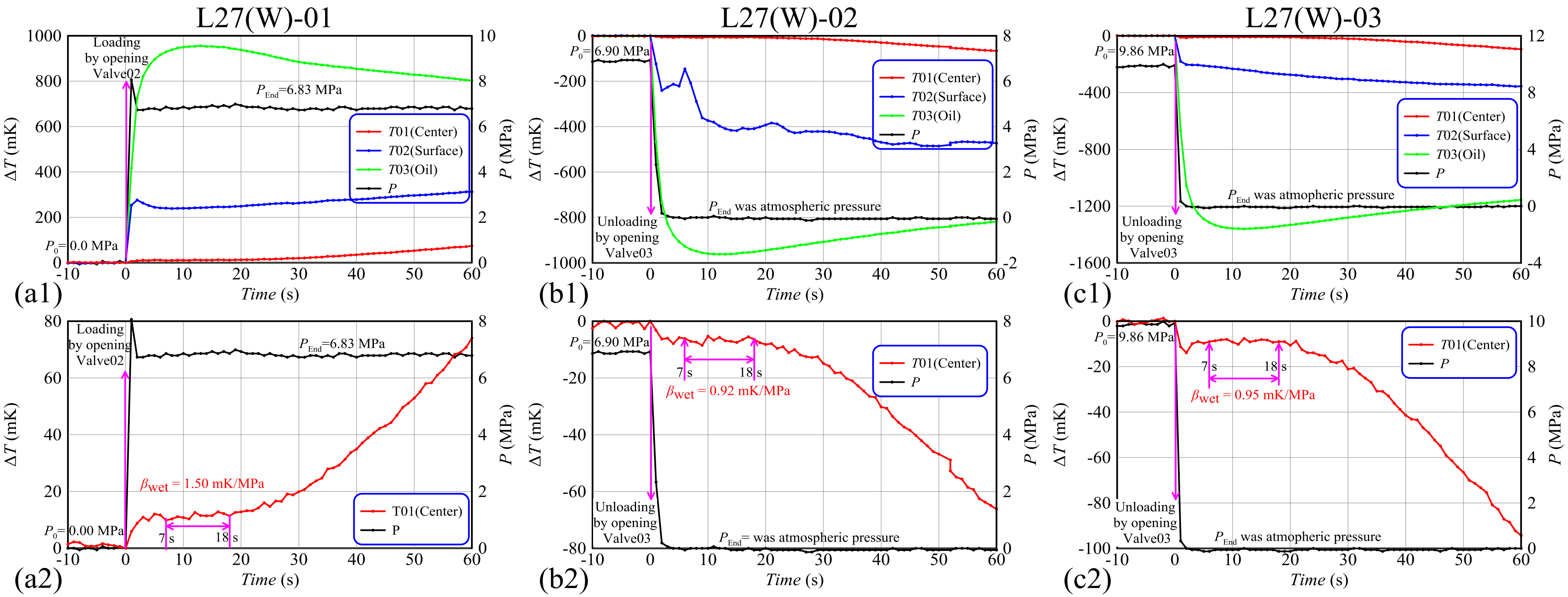

Figure 7. Changes of confining pressure (ΔP, in Vessel B) and temperature (ΔT) during the loading/unloading processes of water-saturated Longmensan limestone (L27(W)) under quasi-drained conditions.

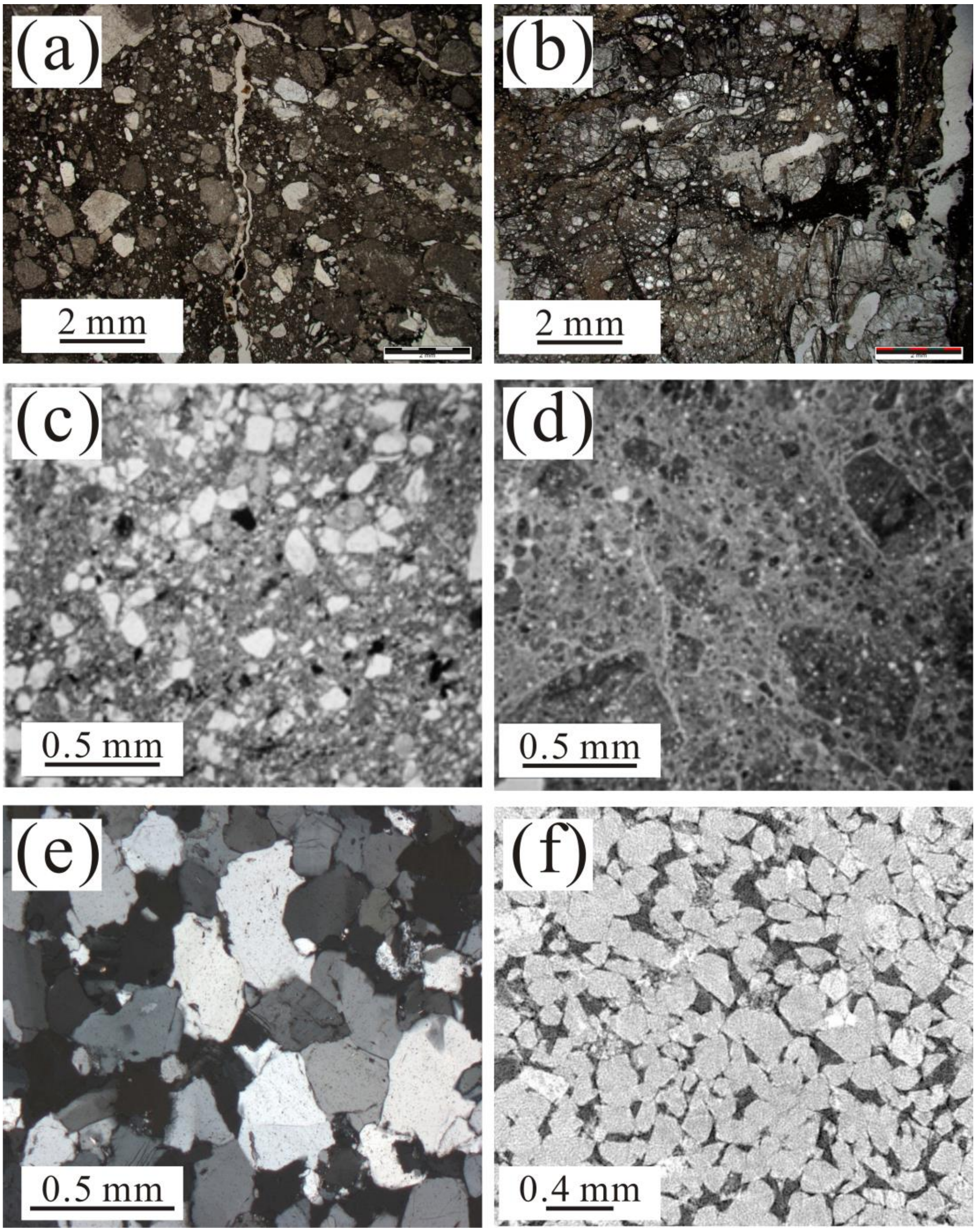

Figure 8. (a-b) Photomicrographs of thin sections (in polarized light) of cataclasite and fault breccia from the Longmenshan Fault Zone [*Wang et al.*, 2014]. (c-d) Photomicrographs of thin sections of fault breccia and gouge from the Chelungpu Fault Zone [*Hashimoto et al.*, 2007]. (e) Photomicrograph of thin section (in crossed polars) of Rajasthan sandstone (RJS) from India (provided by Takehiro Hirose). (f) Cross-section of micro-CT image of Berea sandstone (BRS) from the U. S. [*Dong*, 2008].

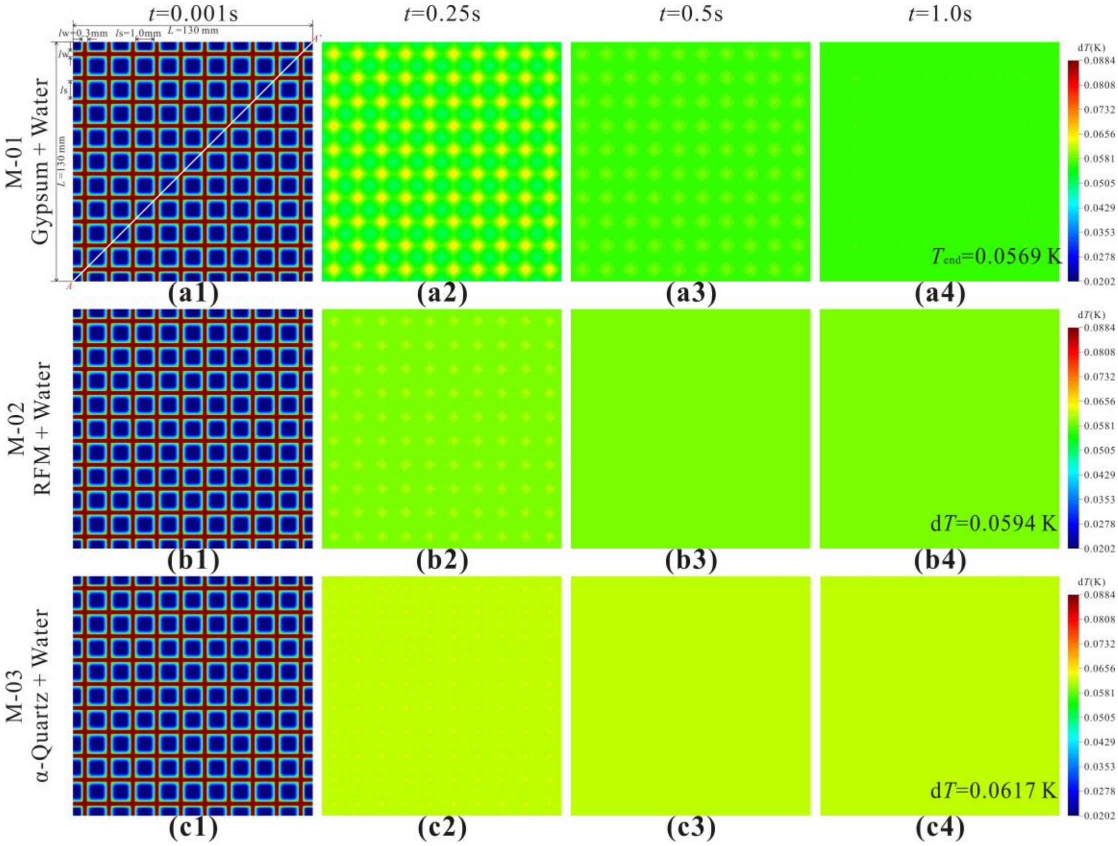

Figure 9. Temperature evolution characteristics of water-saturated rocks with different minerals after instantaneous loading from 0 MPa to 10 MPa (i.e., ΔP_c = 10 MPa). In models M-01, -02 and -03, the solid grains were gypsum (κ_{Gypsum} = 0.51 mm^2/s), main rock-forming minerals averaged (RFM, κ_{RFM} = 2.08 mm^2/s) and α-quartz ($\kappa_{\alpha\text{-quartz}}$ = 4.15 mm^2/s), respectively. In these models, each solid grain is surrounded by pore water and the equivalent porosity is up to 0.408 (i.e., ϕ = 0.408) since the sizes of grains and pores are set to be 1.0 mm and 0.3 mm, respectively. Each model was meshed to 11025 quadrilateral elements with the spatial resolution of 0.2 mm for grains and 0.06 mm for pores, respectively. The time resolution is up to dt = 0.001 s. (a1-a4) Temperature distribution in model M-01 at t = 0.001 s, 0.25 s, 0.5 s and 1.0 s, respectively. (b1-b4) Temperature distribution in model M-02 at t = 0.001 s, 0.25 s, 0.5 s and 1.0 s, respectively. (c1-c4) Temperature distribution in model M-03 at t = 0.001 s, 0.25 s, 0.5 s and 1.0 s, respectively. The temperature profiles along line A-A' in the three models at t = 0.001 s, 0.25 s, 0.5 s, 0.75 s and 1.0 s, are illustrated in Figure S2.

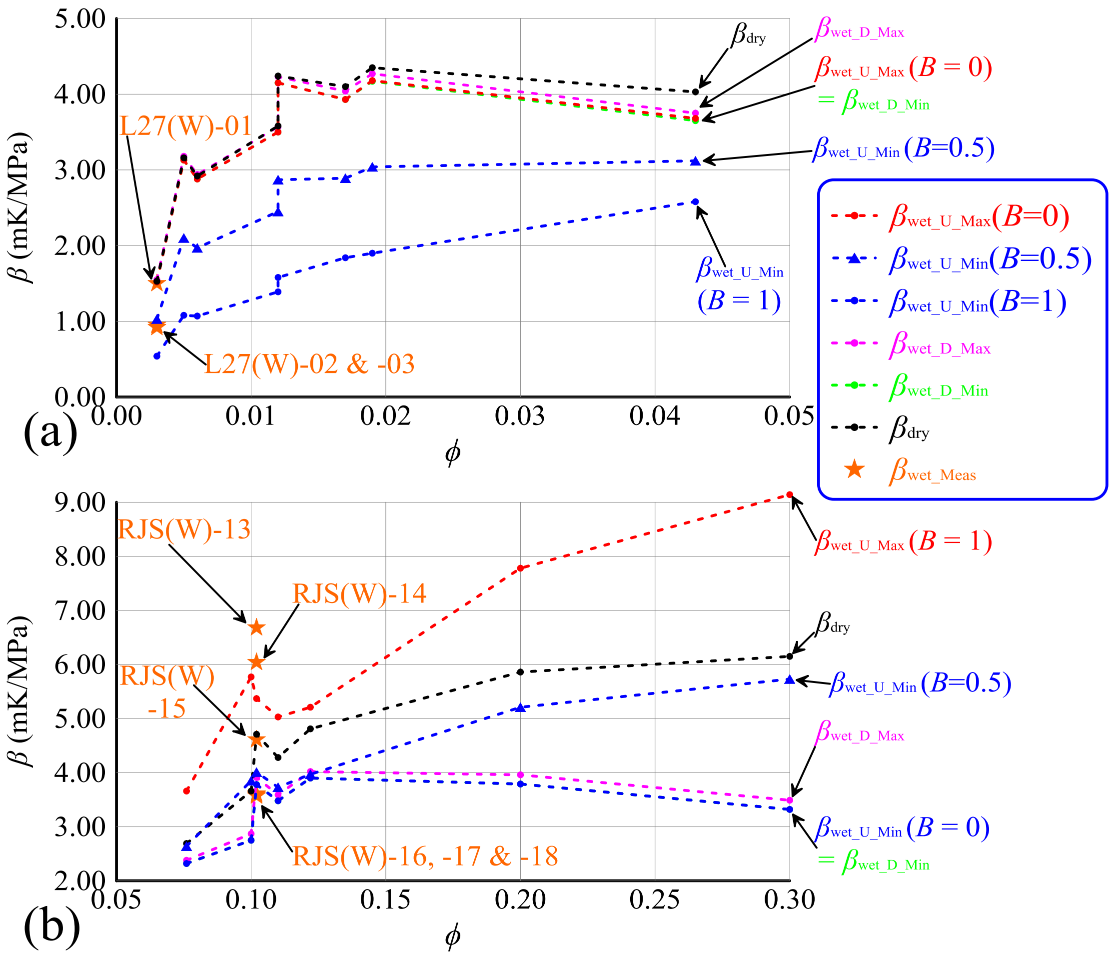

Figure 10. Calculated lower and upper limits of β_{wet} for all 15 rock samples when (a) Porosity (ϕ) is within 0.05 and (b) porosity (ϕ) ranges from 0.05 to 0.30. Red and pink circles represent the upper limits under undrained ($\beta_{\mathrm{wet\_U\_Max}}$) and drained ($\beta_{\mathrm{wet\_D\_Max}}$) conditions, respectively. Blue and green circles represent the lower limits in both undrained ($\beta_{\mathrm{wet\_U\_Min}}$) and drained ($\beta_{\mathrm{wet\_D\_Min}}$) conditions, respectively. Pink dots represent $\beta_{\mathrm{wet\_U}}$ when B is 0.5 ($\beta_{\mathrm{wet\_U}}(B{=}0.5)$). Blue triangles represent the lower limit under undrained conditions with Skempton's coefficient $B = 0.5$. Black circles represent the measured β of dry rocks (β_{dry}) [*Yang et al.*, 2017]. Orange stars denote measured values of β_{wet} in tests RJS(W)-13 to -18 and L27(W)-01 to -03.

Journal of Geophysical Research: Solid Earth

Supporting Information for

Theoretical and experimental analyses of temperature responses of water-saturated rocks to changes in confining pressure

Xiaoqiu Yang[1, 2], Weiren Lin[3], Hehua Xu[1, 2], Osamu Tadai[4], Xin Zeng[1, 2]

[1]Key Laboratory of Ocean and Marginal Sea Geology, South China Sea Institute of Oceanology, Innovation Academy of South China Sea Ecology and Environmental Engineering, Chinese Academy of Sciences, Guangzhou 511458, China

[2]Southern Marine Science and Engineering Guangdong Laboratory (Guangzhou), Guangzhou 511458, China

[3]Graduate School of Engineering, Kyoto University, Kyoto 615-8540, Japan

[4]Marine Works Japan Ltd., Nankoku 783-8502, Japan

Corresponding author:

Xiaoqiu Yang (yxq2081@scsio.ac.cn), ORCID ID: 0000-0002-3113-8796

Contents of this file

Figures S1, S2, S3 and S4

Tables S3, S4

A brief review of the theory of thermo-poroelasticity

Detailed descriptions about the measurement system

Detailed descriptions about the experimental procedure

Thermal equilibrium between the skeletal framework and the pore fluid

Additional Supporting Information Files uploaded separately

Captions for Tables S1 and S2, Movies S1, S2, and S3

Introduction

This supporting file provides the Figures S1, S2, S3 and S4, Tables S1, S2, S3 and S4, Movies S1, S2 and S3, Brief review of the theory of thermo-poroelasticity, Detailed descriptions about the measurement system, Detailed descriptions about the experimental procedure, and Thermal Equilibrium between the skeletal framework and the pore fluid.

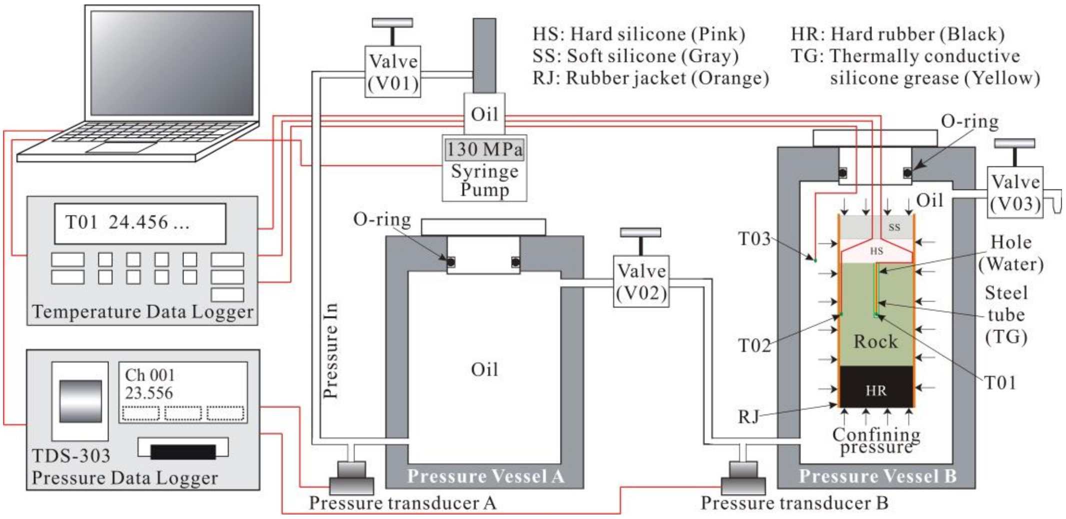

Figure S1. Schematic diagram of the new hydrostatic compression system improved from *Yang et al.* [2017] and used in this study for measuring the adiabatic pressure derivative of the temperature for water-saturated rock specimens (β_{wet}). The system consists of two pressure vessels with a servo-controlled pump that provides pressure up to 130 MPa. The sample assembly is placed in Pressure Vessel B. Three temperature sensors (T01 in sample center, T02 on sample surface and T03 in oil around the rock specimen in the Pressure Vessel B) were deployed for monitoring temperature changes during rapid loading/unloading processes, along with a temperature data logger and a confining pressure data logger.

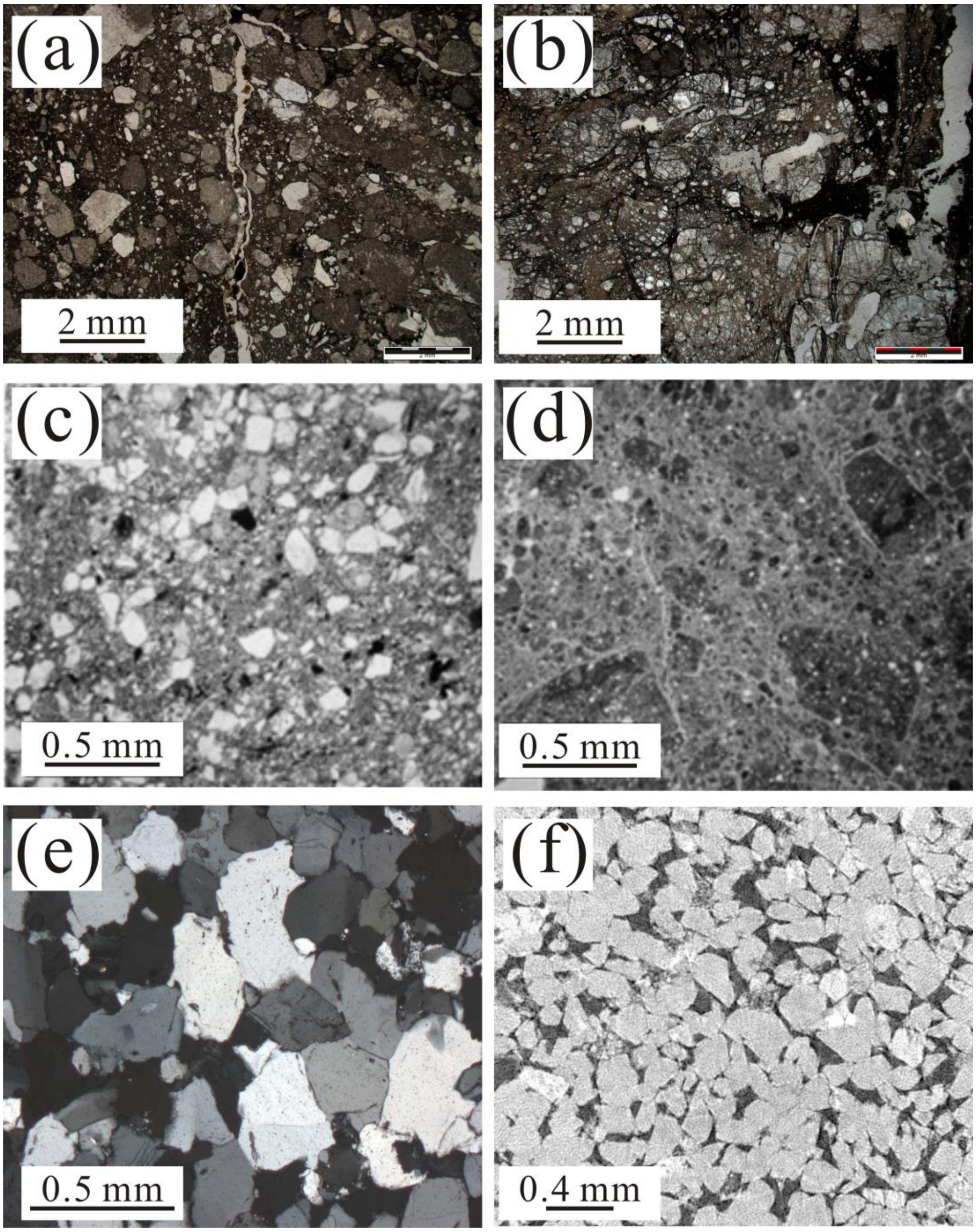

Figure S2. (a-b) Photomicrographs of thin sections (in polarized light) of cataclasite and fault breccia from the Longmenshan Fault Zone [*Wang et al.*, 2014]. (c-d) Photomicrographs of thin sections of fault breccia and gouge from the Chelungpu Fault Zone [*Hashimoto et al.*, 2007]. (e) Photomicrograph of thin section (in crossed polarized light, i.e., under crossed nicol) of Rajasthan sandstone (RJS) from India (provided by Takehiro Hirose). (f) Cross-section of micro-CT image of Berea sandstone (BRS) from the U. S. [*Dong*, 2008].

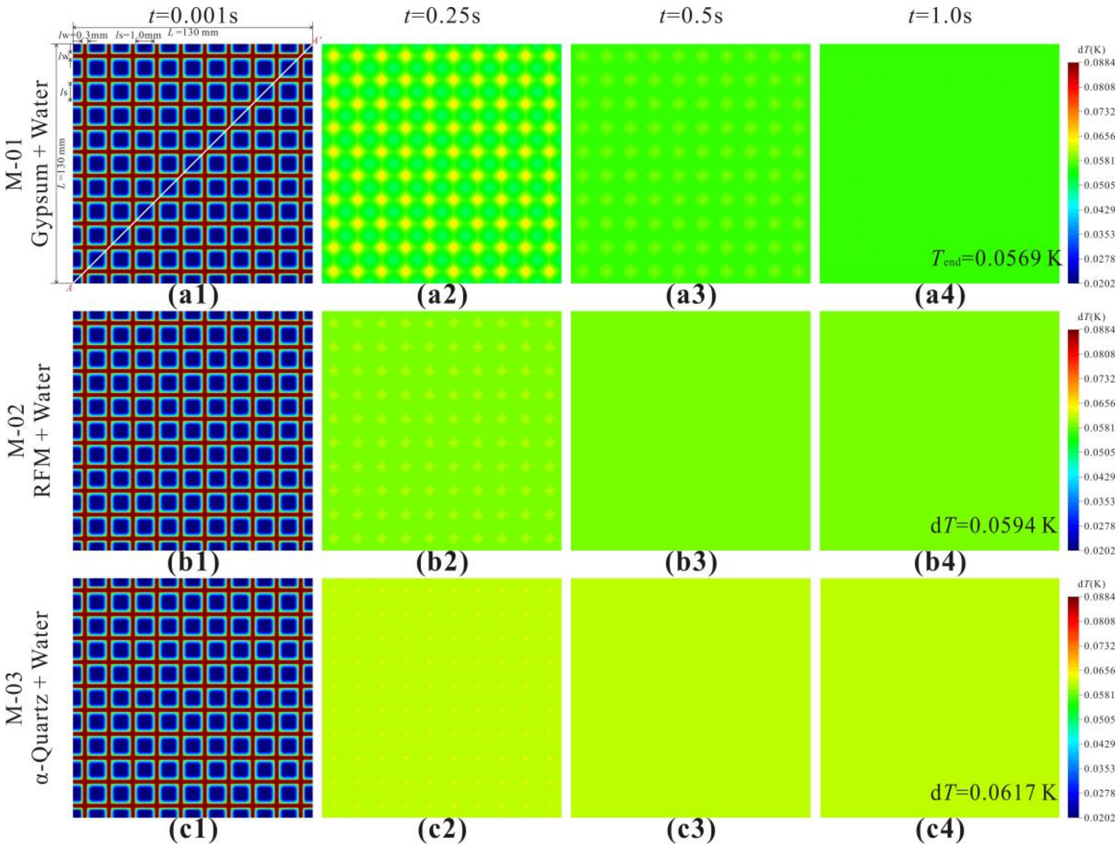

Figure S3. Temperature evolution characteristics of water-saturated rocks with different minerals after instantaneous loading from 0 MPa to 10 MPa (i.e., ΔP_c = 10 MPa). In models M-01, -02 and -03, the solid grains were gypsum (κ_{Gypsum} = 0.51 mm^2/s), main rock-forming minerals averaged (RFM, κ_{RFM} = 2.08 mm^2/s) and α-quartz ($\kappa_{\alpha\text{-quartz}}$ = 4.15 mm^2/s), respectively. In these models, each solid grain is surrounded by pore water, and the equivalent porosity is up to 0.408 (i.e., ϕ = 0.408) since the sizes of grains and pores are set to be 1.0 mm and 0.3 mm, respectively. Each model meshed to 11025 quadrilateral elements with the spatial resolution of 0.2 mm for grains and 0.06 mm for pores, respectively. The time resolution is up to dt = 0.001 s. (a1-a4) Temperature distribution in model M-01 at t = 0.001 s, 0.25 s, 0.5 s and 1.0 s, respectively. (b1-b4) Temperature distribution in model M-02 at t = 0.001 s, 0.25 s, 0.5 s and 1.0 s, respectively. (c1-c4) Temperature distribution in model M-03 at t = 0.001 s, 0.25 s, 0.5 s and 1.0 s, respectively. The temperature profiles along line A-A’ in the three models at t = 0.001 s, 0.25 s, 0.5 s, 0.75 s and 1.0 s, are illustrated in Figure S4.

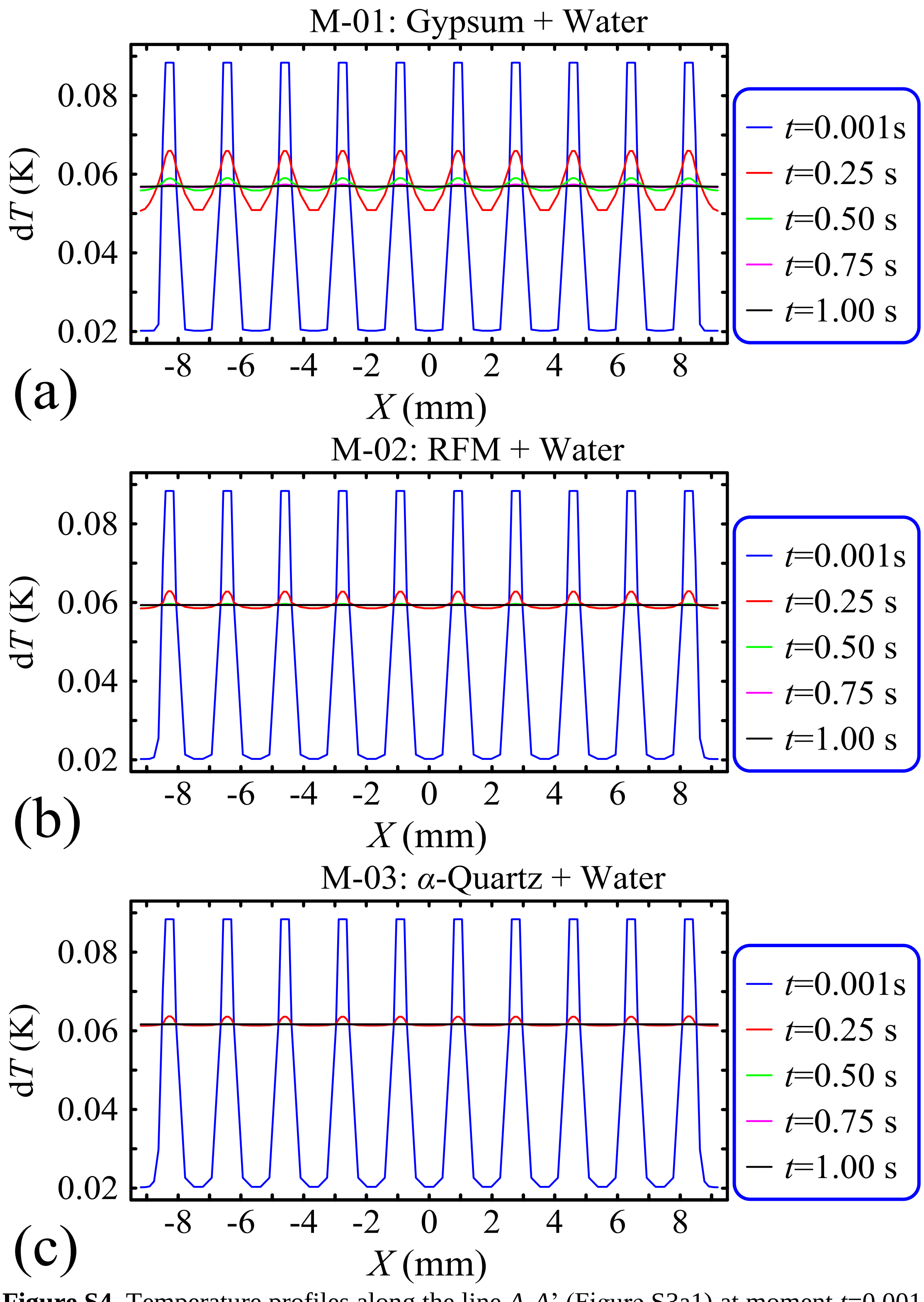

Figure S4. Temperature profiles along the line *A-A*' (Figure S3a1) at moment t=0.001 s, 0.25 s, 0.5 s, 0.75 s and 1.0 s. In models M-01, -02 and -03, the solid grains were gypsum (κ_{Gypsum} = 0.51 mm^2/s), main rock-forming minerals averaged (RFM, κ_{RFM} = 2.08 mm^2/s) and α-quartz ($\kappa_{\alpha\text{-quartz}}$ = 4.15 mm^2/s), respectively.

Table S3. Estimations of Characteristic Distance for Several Main Rock-Forming Minerals in the crust and Water

Mineral/Material	(ρc) (MJ/(m^3·K))	λ (W/(m·K))	κ (mm^2/s)	l (τ'=1 s) (mm)	References
Feldspar (mean value)	1.740	2.30	1.32	1.149	[*Pan*, 1993; *Schön*, 2011]
α-Quartz	1.854	7.69	4.15	2.037	
Mica (muscovite)	2.152	2.30	1.07	1.034	
Amphibole	2.310	2.90	1.26	1.122	
Pyroxene (enstatite)	2.407	4.47	1.86	1.364	
Pyroxene (diopside)	2.196	4.66	2.12	1.456	
Olivine (forsterite)	2.185	5.03	2.30	1.517	
Calcite	2.168	3.59	1.66	1.288	
Main RFMs (averaged)	2.131	4.01	2.08	1.442	
Gypsum	2.466	1.26	0.51	0.714	
Water (at 25°C and 0.1 MPa)	4.169	0.61	0.15	0.387	[*Lide*, 2010]

Note: 1) λ, κ, and (ρc) are thermal conductivity, thermal diffusivity, and volumetric heat capacity, respectively; 2) l (τ'=1 s) is the characteristic distance when the time interval τ' is 1 s; 3) Main RFMs refers to the main rock-forming minerals.

Table S4. Model Parameters of Numerical Simulations on Thermal Equilibrium between Skeletal Framework and pore water

Model	Material	B	α	ΔP_c (MPa)	ΔP_f (MPa)	ΔP^{eff} (MPa)	β_w (mK/MPa)	β_{frm} (mK/MPa)	A_w (W/m^3)	A_{frm} (W/m^3)	T_{end} (K)
M-01	Gypsum+Water	0.5	0.9506	10.0	5.0	5.247	17.68	3.85	368.435	12.330	0.0569
M-02	RFM+Water	0.5	0.9506	10.0	5.0	5.247	17.68	3.85	368.435	10.655	0.0594
M-03	Quartz+Water	0.5	0.9506	10.0	5.0	5.247	17.68	3.85	368.435	9.270	0.0617

Note: here, the Skempton's coefficient is considered to B = 0.5. The effective stress coefficient α was estimated from the porosity (ϕ=0.408) by equation (28). The changes in pore pressure (ΔP_f) and effective pressure (ΔP^{eff}) was calculated with equation (9). The β of the skeletal framework (β_{frm}) was to be 3.85 mK/MPa, which is the mean value of β of dry rocks [*Yang et al.*, 2017]. A_w and A_{frm} are the "heat sources" in pore water and skeletal framework calculated by equation (S8) since the loading was considered to be finished within 0.001 s. T_{end} is the final balance temperature calculated by theoretical equations (9)-(13).

A brief review of the theory of thermo-poroelasticity

In thermoelasticity in general, the mechanical interaction term in the temperature-distribution equation is neglected. In fact, many years ago, *Duhamel* [1837] and *Neumann* [1885] tried to include such an interaction with the argument (for an isotropic substance) that the rate of temperature change was linearly dependent not only on the net rate of heat inflow but also on the rate of dilatation. A detailed discussion of the complete temperature-distribution equation is given by *Biot* [1956]. His equation can be written as

$$\frac{\partial T}{\partial t} = \kappa \frac{\partial^2 T}{\partial t^2} + \frac{K \cdot \alpha_v}{c} \frac{\partial e}{\partial t}, \qquad \text{(S1)}$$

in which, T is temperature, t is time, e is dilatation; κ and c are thermal diffusivity and specific heat, respectively; K and a_v are rock bulk modulus and coefficient of volumetric thermal expansion, respectively. *Lessen* [1956] derived the same equation for a thermoelastic solid from thermodynamical principles. The usual treatment of infinitesimal deformation thermoelastic problems considers the following relations:

Equilibrium: $\rho \frac{\partial^2 u_i}{\partial t} = \sigma_{ki,k} + F_i, \qquad \text{(S2)}$

Generalized Stress-Strain-Temperature Law: $\varepsilon_{ij} = G_{ij,kl}\sigma_{kl} + \alpha_{ij}(T - T_0), \qquad \text{(S3)}$

where u_i is displacement, F_i is body force per unit mass; σ_{ij} and ε_{ij} are stress tensor and strain tensor, respectively; ρ, G_{ijkl} and α_{ij} are density, isothermal elasticity tensor and thermal expansion coefficient tensor, respectively; T and t are temperature and time, respectively. The physical implications of the foregoing ensemble of equations (S1)—(S3) are that, there are not only a thermodynamic interaction term in the generalized stress-strain-temperature law, but also the intuitively expected mechanical interaction term in the temperature-distribution equation [*Lessen*, 1956].

Geertsma [1957a] derived the theory about the effect of fluid pressure decline on volumetric changes of porous rocks and mentioned the thermoelasticity and the elasticity of saturated porous media [*Geertsma*, 1957b], but only discussed the analogous behaviour of the temperature distribution in thermoelastic problems and the liquid pressure distribution in a saturated porous medium [*Geertsma*, 1957b] based on the complete pore pressure-distribution equation [*Biot*, 1941]

$$\frac{1}{Q}\frac{\partial p}{\partial t} = \beta \frac{\partial^2 p}{\partial t^2} - \alpha \frac{\partial e}{\partial t}, \qquad \text{(S4)}$$

which is in structure identical with the complete temperature-distribution equation (S1).

In Equation (S4), p is pore pressure, t is time, e is dilatation, Q and a are not simple measurable physical quantities as in the corresponding temperature-distribution equation (S1). *Norris* [1992] discussed the correspondence between poroelasticity and thermoelasticity too. He found that an interesting and useful analogy can be drawn between the equations of static poroelasticity and the equations of thermoelasticity including entropy. The correspondence is of practical use in determining the effective parameters in an inhomogeneous poroelastic medium using known results from the literature on the effective thermal expansion coefficient and the effective heat capacity of a disordered thermoelastic continuum.

Zimmerman [2000] also briefly derived the equations of linearised poroelasticity and thermoelasticity. His derivation results are the same as the complete pore pressure-distribution equation (S4) [*Biot*, 1941] and the complete temperature-distribution equation (S1) [*Biot*, 1956], respectively. Based on these equations, he presented the dimensionless parameters that quantify the strength of the coupling between mechanical and hydraulic (or thermal) effects. The results show that the poroelastic coupling parameter is shown to be the product of the Biot coefficient and the Skempton coefficient; the thermoelastic coupling parameter can be interpreted as the ratio of stored elastic strain energy to stored thermal energy. For liquid-saturated rocks, the poroelastic coupling parameter usually lies between 0.1 and 1.0, which means that the mechanical deformation has a strong influence on the pore pressure. The thermoelastic coupling parameter is usually very small, so that, although the temperature field influences the stresses and strains, the stresses and strains do not appreciably influence the temperature field.

McTigue [1986, 1990] given the constitutive equations of the linear theory of thermos-poroelasticity as

$$\begin{cases} \varepsilon_{ij} = \frac{1}{2G}\left[\sigma_{ij} - \frac{1}{1+v}\sigma_{ij}\delta_{ij}\right] + \frac{\alpha(1-2v)}{2G(1+v)}\delta_{ij}p + \frac{\beta_s}{3}\delta_{ij}pT \\ \zeta = \frac{\alpha(1-2v)}{2G(1+v)}\sigma_{kk} + \frac{\alpha^2(1-2v)^2+(1+v_u)}{2G(1+v)(v_u-v)}p - \phi(\beta_f - \beta_s)T \end{cases}, \qquad \text{(S5)}$$

where $\varepsilon_{\mathrm{ij}}$ is the change of strain of the rock, σ_{ij} is the change of stress of the rock (tension positive), p, T and ζ are the change of pore pressure, temperature and pore volume, respectively. The rock property constants are as follows: α is *Biot*'s coefficient, v and v_u are the drained and undrained Poisson's ratios, G is the bulk shear modulus, B is Skempton's pore pressure coefficient, β_s and β_f are the volumetric thermal expansion coefficient of the solid and the pore fluid, respectively. This theory was used to study the mechanical stability of geothermal reservoirs during cold water injection [*Simone*, 2013] and the role of thermo-poromechanical processes on reservoir seismicity and permeability enhancement [*Ghassemi & Tao*, 2016]. Recently, the fully coupled thermal-hydraulic-mechanical model and finite element model, which are similar to *McTigue's* theory, were presented for heat and gas transfer in thermal stimulation enhanced coal seam gas recovery [*Teng et al.*, 2018], and fractured geothermal reservoirs [*Salimzadeh et al.*, 2018], respectively.

Based on the above brief review about the thermoelasticity, poroelasticity and the coupling on the thermo-poroelasticity, we can found that all the prior researches focus on either the temperature field influences the stresses/strains [*Carlson*, 1973; *Wong and Brace*, 1979; *Nowacki*, 1986; *Wang et al.*, 1989; *Hetnarski and Eslami*, 2008], or stresses/strains influence the temperature field of thermoelastic solids [*Duhamel*, 1837; *Neumann*, 1885; *Biot*, 1956; *Lessen*, 1956; *Boley and Weiner*, 1960] and pore pressure of porous rocks [*Biot*, 1941; *Geertsma*, 1957a], respectively. But up to now, a clear understanding of the temperature response of fluid-saturated porous rocks to changes in stresses and strains has been lacking. It means that we know very little about how the stresses and strains influence the temperature field of the fluid-saturated rocks. Consequently, in this study, we try to derive the theoretical basis about the temperature response of fluid-saturated porous rocks to changes in stresses and strains during the adiabatic process, and then carry out systematic experiments under undrained and drained conditions.

Detailed descriptions about the measurements system

To measure β_{wet}, we improved the hydrostatic compression system used to measure β_{dry}. Figure S1 shows the improved system with two pressure vessels and a servo-controlled pump that provides a pressure of up to 130 MPa at room temperature. Both pressure vessels are filled with silicone oil as the pressure medium. To avoid oil permeating into the pores of the rock sample, there are two dielectric silicone and rubber end pieces, each 50 mm in height, at the top and bottom of the rock specimen. The silicone end piece includes two parts, each 25 mm thick (Figures S1, 3a and 4a). One is hard silicone. The other is soft silicone, which is made of two original silicone components produced by Shin-Etsu Chemical Co., Ltd.

All of the silicone and rubber end pieces are 50 mm in diameter, like the rock specimen. We enveloped them together with a rubber jacket and three O-rings on each end piece. One O-ring is between the hard silicone/rubber end piece and the rubber jacket. Two are around the outside of the rubber jacket (Figure 3a, 3e). We drilled a hole that was 2.8 mm in diameter (D_h) and 26.0 mm in depth (H) in the center of each rock specimen (Figures S1, 3 and 4). Then, we installed temperature sensors (PT1000 M213 Class-B, one kind of platinum resistance temperature detector produced by the Heraeus Sensor Technology GmbH, Kleinostheim, Germany) through the top silicone end piece in the center (T01) and on the surface (T02) of the sample in addition to a temperature sensor in the oil (T03) (Figures S1, 3 and 4). The three temperature sensors were connected to the temperature data logger, which we designed based on a bridge reversal excitation circuit with a high temperature resolution of ~1.0 mK at room temperature [*Qin et al.*, 2013]. There is a pressure transducer (PG-2TH, Kyowa electronic instruments, Co.Ltd, Tokyo, Japan) which is connected to a pressure data logger (TDS-303, Tokyo Sokki Kenkyujo Co. Ltd, Tokyo, Japan). The sampling intervals of temperature and pressure are 1 s. Thus, during the rapid loading and unloading processes, we can monitor the confining pressure (oil pressure, P) and temperature changes of the rock specimen and oil with the pressure and temperature data loggers with a data sampling interval of 1 s.

Detailed descriptions about the experimental procedure

To saturate the porous rock specimens, they were placed in a cup filled with ion-exchanged water, and then, they were placed in a vacuum chamber and vacuumed for more than 6 days. During this time, all of the air was removed from the pores, and the pores were saturated with water. For the quasi-undrained conditions, a steel tube with a miniature temperature sensor T01 was placed into the central hole in the specimen (Figures 3a–3c). For the quasi-drained conditions, only a miniature temperature sensor T01 was installed in the central hole (Figure 4). Then, the sample assembly was put together as shown in Figures 3 and 4 and was placed into Vessel B (Figure S1).

The new hydrostatic compression system, which was improved from a previous system for use in this study, was to accomplish the rapid loading and unloading (Figure S1). For the rapid loading experiments, there were three main steps: (1) valves V02 and V03 were closed, while valve V01 was left open (Figure S1); (2) the confining pressure in Vessel A was increased to a predetermined pressure (e.g., 125 MPa) using the servo-controlled pump, while the confining pressure in Vessel B was kept constant at a lower pressure (e.g., ~0–2 MPa) and at room temperature for at least 4 hours to allow the system to achieve thermal equilibrium; and (3) the rock specimen was rapidly loaded by manually opening valve V02. The confining pressures in Vessels A and B would immediately trend to the same value after valve V02 was opened.

For the rapid unloading, there are also three main steps: (1) valve V03 was closed, while valves V01 and V02 were kept open; (2) the confining pressures in Vessels A and B were increased to a predetermined pressure (e.g., 10 MPa) using the servo-controlled pump and were kept constant at room temperature for at least 4 hours to enable the system's temperature to reach equilibrium; and (3) valve V02 was manually closed, and valve V03 was opened to instantaneously unload the confining pressure in Vessel B to atmospheric pressure (~0.1 MPa). The key experimental records and results are presented in Table 3. In this study, the maximum confining pressure in Vessel B was set as ~15 MPa, which is much lower than the strength of the rocks, to prevent any influence of stress loading on the temperature response during multiple tests of the same rock specimen.

Thermal equilibrium between the skeletal framework and the pore fluid

Whether under undrained or drained conditions, the temperature change of the skeletal framework is distinct from that of the pore fluid at the initial moment of rapid loading/unloading, which is demonstrated by Equations (11) and (21) (i.e., $\Delta T_{\mathrm{frm}} \neq \Delta T_{\mathrm{f}}$). However, using Equations (13) and (26), we obtain the apparent temperature change of the fluid-saturated porous rock (ΔT) based on the fact that thermal equilibrium between the skeletal framework and pore fluid can be achieved within the data sampling interval (i.e., 1 s) after instantaneous loading/unloading. In this section, we investigate the thermal equilibrium using the estimated characteristic distance and numerical simulation.

1) Estimation of characteristic distance

Through dimensional analysis of the heat conduction equation, we can obtain the fact that if the temperature changes occur within a characteristic time interval τ, they will propagate a distance on the order of

$$l = \sqrt{k\tau}, \qquad \text{(S6)}$$

where κ is thermal diffusivity. Similarly, a time,

$$\tau = l^2/k, \qquad \text{(S7)}$$

is required for the temperature changes to propagate a distance l [*Turcotte and Schubert*, 2014]. Such a simple consideration can be used to obtain useful estimations of the thermal effects and the thermal equilibrium that occur in porous rocks during rapid loading/unloading processes.

There are currently around 4170 known mineral species. Among these minerals, approximately 50 are common rock-forming minerals. Silicates are the most abundant group of minerals. They constitute over 90% of the Earth's crust. The feldspar group represents about 60% of these crustal minerals, while silica (mainly quartz) represents 10% to 13% [*Demange*, 2012]. Table S2 lists the thermal properties of 52 common rock-forming minerals [*Pan*, 1993; *Schön*, 2011]. Pyrite has the greatest thermal diffusivity (κ_{pyrite} = 7.66 mm^2/s), while gypsum has the lowest thermal diffusivity (κ_{gypsum} = 0.51 mm^2/s). The main rock-forming minerals in the crust are quartz, orthoclase, plagioclase, mica, amphibole, pyroxene, olivine, and calcite [*Xiao et al.*, 2017]. Consequently, we estimated the characteristic distances for several main rock-forming minerals and water using Equation (S6) and the known thermal diffusivities

(Tables S2, S3). The thermal properties of rock-forming minerals and estimations of thermal characteristic time/distance are also stored and provided in Zenodo (http://doi.org/10.5281/zenodo.4242969). The results indicate that temperature changes can propagate 1.0–2.0 mm in most of the main rock-forming minerals within the data sampling interval of 1 s used in this study. Even if the thermal diffusivity is as low as those of gypsum (κ_{gypsum} = 0.51 mm^2/s) and water (κ_{water} = 0.15 mm^2/s), the characteristic distances (when τ' = 1 s) can reach up to 0.714 mm and 0.387 mm, respectively (Figure S2).

Generally, for most porous rocks in the crust, the sizes of the solid grains, i.e., rock-forming minerals, and pores are limited. Figure S2 shows photomicrographs of thin sections of fault rocks (cataclasite, breccia, and gouge) from the Longmenshan Fault Zone (a-b), the Chelungpu Fault Zones (c-d), the Rajasthan sandstone (RJS) from India (e), and a cross-section of micro-CT image of the Berea sandstone (BRS) from the U.S. (f). Except for the RJS and the BRS, most of the rocks used in this study were collected from the Longmenshan and Chelungpu Fault Zones (Table 2). Thus, the internal structures of the crustal rocks shown in Figure S2 have certain representativeness in this study. They indicate that the sizes of the solid grains in porous rocks are usually within ~1.0 mm, which are less than the characteristic distances for 1 s in most of the main rock-forming minerals. In addition, even if the porosity is up to 0.2, e.g., in the BRS (i.e., ϕ = 0.2), the sizes of the pores are usually less than 0.2 mm, which is about half of the characteristic distance for 1 s in water (l = 0.387 mm, Figure S2). In other words, the solid grains and pore water can approximately reach thermal equilibrium through heat conduction within 1 s after instantaneous loading/unloading.

2) Numerical simulation

Based on the above investigation on the sizes of the solid grains and pores in rocks, we modeled the internal structure of water-saturated rock, in which each solid grain is surrounded by pore water, and the sizes of the solid grains and pores are up to 1.0 mm and 0.3 mm, respectively (Figure S3a1). In this case, the equivalent porosity is up to 0.408 (i.e., ϕ = 0.408).

To have a clear understanding of the thermal equilibrium reached between the grains and the pore water, a heat conduction finite element model framed within a two-dimensional Cartesian coordinate system (2dxy) was constructed. The heat conduction equation for the 2dxy system is

$$\begin{cases} (\rho c)\dfrac{\partial T}{\partial t} = \lambda\left(\dfrac{\partial^2 T}{\partial x^2} + \dfrac{\partial^2 T}{\partial y^2}\right) + A \\ A = \beta(\rho c)\dfrac{\partial P}{\partial t} \\ T(x, y, 0) = 0 \end{cases}, \qquad \text{(S8)}$$

Where λ is the thermal conductivity; (ρc) is the volumetric heat capacity; and β is the adiabatic pressure derivative of the temperature. A is the heat source term driven by the change in confining pressure during loading/unloading processes. The initial condition $T(x,y,0)$ is set as 0 since the entire rock specimen assembly achieves thermal equilibrium before loading/unloading (see the Detailed descriptions about the experimental procedure in supporting information).

Here, taking the following process as an example: the confining pressure increases from air pressure to 10 MPa within dt=0.001 s under undrained conditions (i.e., ΔP_c = 10 MPa), and Skempton's coefficient is considered to B = 0.5. According to Equation (9), the changes in the pore pressure (ΔP_f) and the effective pressure (ΔP^{eff}) can be calculated since the effective stress coefficient α can be estimated from the equivalent porosity (ϕ=0.408) using equation (28). The estimated α, the calculated ΔP^{eff} and ΔP_f are listed in Figure S3. After setting the β of the skeletal framework (β_{frm}) to 3.85 mK/MPa, which is the mean value of β for dry rocks [*Yang et al.*, 2017], we solved the temperature field evolution after rapid loading when the solid grains are gypsum, an average of the main rock-forming minerals (RFM), and α-quartz in models M-01, -02, and -03, respectively (Figure S3). The time step was 0.001 s in these models. The thermal properties of gypsum, RFM, α-quartz and water are listed in Table S3. Figure S3 shows the thermal equilibrium process between the grains and the pore water at t=0.001 s, 0.25 s, 0.5 s, and 1.0 s after rapid loading. First, taking model M-01 as an example, at the initial moment of rapid loading (t=0.001 s), the temperature increases 0.0202 K within the solid grains (gypsum), but 0.0884 K in the pore water (Figure S3a1). There is a still temperature difference between the grains and the pore water at t=0.25 s (Figure S3a2). However, the temperature difference becomes very small after 0.5 s (Figure S3a3). At t=1.0 s, both the temperature within grains and the pore water trend to 0.0569 K, which is the same as the final balance temperature T_{end} calculated by theoretical Equations (9)-(13) (Figure S3a4 and Table S4). It is worth noting that gypsum has the lowest thermal diffusivity (κ_{gypsum}=0.51 mm^2/s) of the main RFMs (Table S2). This means that the thermal equilibrium time will be shorter than 1.0 s since the thermal diffusivity of the grains is higher than κ_{gypsum}. For example, in models M-02 and -03, the samples almost reach thermal equilibrium after 0.5 s (Figures S3b3 and S3c3) because the thermal diffusivities of the RFM and the α-quartz are up to 2.08 mm^2/s and 4.15 mm^2/s, respectively (Table S3). Figure S4 shows the temperature profiles along line *A*-*A*' (Figure S3a1) at *t*=0.001 s, 0.25 s, 0.5 s, 0.75 s, and 1.0 s. It also shows that 1.0 s is enough for the water-saturated rocks to achieve thermal equilibrium after the confining pressure changing. In addition, Movies S1, S2, and S3 (in the Supporting Information) provide very clear images and processes to understand the inner temperature evolution of the entire water-saturated rock specimen within 1.0 s after instantaneous loading. Movies S1, S2, and S3 are also deposited in Zenodo (http://doi.org/10.5281/zenodo.4242969).

From the above characteristic distance analysis and numerical simulation, the results reveal that water-saturated rocks can reach achieve thermal equilibrium within 1.0 s after the confining pressure changes.

Table S1. Temperature response of water-saturated Longmenshan limestone (L27) and Rajastan sandstone (RJS) to changes in confining pressure under drained/undrained conditions

Table S2. Thermal Properties of Rock-forming Minerals and Estimations of Characteristic Time/Distance

Movie S1. Internal temperature evolution of the water-saturated sample within 1 s after instantaneous loading in model M-01. Here the solid grains are set to be gypsum with κ_{Gypsum} = 0.51 mm^2/s. In the movie, “u”, the title of the legend, means the temperature change (d*T*) with the unit of K. The temperature evolution starts from *t*=0 s (the time point of instantaneous loading) to t=1 s. The time step is 0.001 s. Thus there are a total of 1000 computational steps. It means at the “step 1”, “step 500” and “step 1000” in the movie are *t*=0.001 s, *t*=0.5 s and *t*=1.0 s, respectively, after instantaneous loading.

“unoda0” is the name of the temperature field in the finite element model (similarly hereafter).

Movie S2. Internal temperature evolution of the water-saturated sample within 1 s after instantaneous loading in model M-02. Here the solid grains are set to be main rock-forming minerals averaged (RFM) with κ_{RFM} = 2.08 mm^2/s.

Movie S3. Internal temperature evolution of the water-saturated sample within 1 s after instantaneous loading in model M-03. Here the solid grains are set to be α-quartz with $\kappa_{\alpha\text{-quartz}}$ = 4.15 mm^2/s.

References

Biot, M. A. (1941), General Theory of Three‐Dimensional Consolidation, Journal of Applied Physics, 12(2), 155-164, doi:10.1063/1.1712886.

Biot, M. A. (1956), Thermoelasticity and Irreversible Thermodynamics, Journal of Applied Physics, 27(3), 240-253, doi:10.1063/1.1722351.

Carlson D.E. (1973) Linear Thermoelasticity. In: Truesdell C. (eds) Linear Theories of Elasticity and Thermoelasticity. Springer, Berlin, Heidelberg. https://doi.org/10.1007/978-3-662-39776-3_2.

De Simone, S., V. Vilarrasa, J. Carrera, A. Alcolea, and P. Meier (2013), Thermal coupling may control mechanical stability of geothermal reservoirs during cold water injection, Physics and Chemistry of the Earth, Parts A/B/C, 64, 117-126, doi:10.1016/j.pce.2013.01.001.

Demange, M. (2012), Mineralogy for petrologists : optics, chemistry, and occurrence of rock-forming minerals, edited, CRC Press, London, doi:10.1201/9780429355172.

Dong, H. (2008), Micro-CT imaging and pore network extraction, Ph.D. thesis, Imperial College London.

Duhamel JMC (1837), Second mémoire sur les phénomènes thermo-mécaniques Second memoir on thermo-mechanical phenomena, Journal de l’Ecole Polytechnique, Tome 15, Cahier 25, pp 1–57.

Geertsma J. (1957a), The effect of fluid Pressure decline on volumetric Changes of porous rocks，Petroleum Transactions, AIME, 210, 331-340.

Geertsma, J. (1957b), A remark on the analogy between thermoelasticity and the elasticity of saturated porous media, Journal of the Mechanics and Physics of Solids, 6(1), 13-16, doi: 10.1016/0022-5096(57)90042-X.

Ghassemi, A., and Q. Tao (2016), Thermo-poroelastic effects on reservoir seismicity and permeability change, Geothermics, 63, 210-224, doi: 10.1016/j.geothermics.2016.02.006.

Hashimoto, Y., K. Ujiie, A. Sakaguchi, and H. Tanaka (2007), Characteristics and implication of clay minerals in the northern and southern parts of the Chelung-pu fault, Taiwan, Tectonophysics, 443(3), 233-242.

Hetnarski, R. B., and M. R. Eslami (2008), Thermal Stresses—Advanced Theory and Applications (Solid Mechanics and Its Applications), Springer, Netherlands, doi:https://doi.org/10.1007/978-3-030-10436-8.

Lessen, M. (1956), Thermoelasticity and thermal shock, Journal of the Mechanics and Physics of Solids, 5(1), 57-61, doi:https://doi.org/10.1016/0022-5096(56)90007-2.

Lide, D. R. (2010), CRC handbook of chemistry and physics, 90th Edition (CD-ROM Version 2010), CRC press/Taylor and Francis, Boca Raton, Fla.

McTigue, D. (1986), Thermoelastic response of fluid‐saturated porous rock, Journal of Geophysical Research: Solid Earth (1978–2012), 91(B9), 9533-9542.

McTigue, D. F. (1990), Flow to a heated borehole in porous, thermoelastic rock: Analysis, Water Resources Research, 26(8), 1763-1774, doi:10.1029/WR026i008p01763.

Neumann F (1885), Vorlesung über die Theorie des Elasticität der festen Körper und des Lichtäthers. Teubner, Leipzig (Meyer, Breslau).

Norris, A. (1992), On the correspondence between poroelasticity and thermoelasticity, Journal of Applied Physics, 71(3), 1138-1141, doi:10.1063/1.351278.

Nowacki, W. (1986), Thermoelasticity, 2nd ed., PWN-Polish Scientific Publishers, Warsaw, and Pergamon Press, Oxford, doi:10.1016/C2013-0-03247-1.

Pan, Z. (1993), Crystallography and mineralogy, 3rd Edition [in Chinese], Geological Publishing House, Beijing.

Qin, Y., X. Yang, B. Wu, Z. Sun, and X. Shi (2013), High resolution temperature measurement technique for measuring marine heat flow, Sci. China Technol. Sci., 56(7), 1773-1778, doi:10.1007/s11431-013-5239-9.

Salimzadeh, S., A. Paluszny, H. M. Nick, and R. W. Zimmerman (2018), A three-dimensional coupled thermo-hydro-mechanical model for deformable fractured geothermal systems, Geothermics, 71, 212-224, doi:10.1016/j.geothermics.2017.09.012.

Schön, J. H. (2011), Physical properties of rocks: a workbook, Elsevier, Oxford.

Teng, T., Y. Zhao, F. Gao, J. G. Wang, and W. Wang (2018), A fully coupled thermo-hydro-mechanical model for heat and gas transfer in thermal stimulation enhanced coal seam gas recovery, International Journal of Heat and Mass Transfer, 125, 866-875, doi:10.1016/j.ijheatmasstransfer.2018.04.112.

Turcotte, D., and G. Schubert (2014), Geodynamics, 3rd ed., Cambridge University Press, Cambridge, U. K.

Wang, H. F., B. P. Bonner, S. R. Carlson, B. J. Kowalls, and H. C. Heard (1989), Thermal stress cracking in granite, Journal of Geophysical Research, 94(B2), 1745-1758.

Wang, H., H. Li, J. Si, Z. Sun, and Y. Huang (2014), Internal structure of the Wenchuan earthquake fault zone, revealed by surface outcrop and WFSD-1 drilling core investigation, Tectonophysics, 619–620, 101-114, doi:10.1016/j.tecto.2013.08.029.

Wong, T.-f., and W. Brace (1979), Thermal expansion of rocks: some measurements at high pressure, Tectonophysics, 57(2), 95-117.

Xiao, Y., R. Zheng, and J. Deng (2017), Petrology introduction, 4th Edition [in Chinese], Geological Publishing House, Beijing.

Yang, X., W. Lin, O. Tadai, X. Zeng, C. Yu, E.-C. Yeh, H. Li, and H. Wang (2017), Experimental and numerical investigation of the temperature response to stress changes of rocks, *Journal of Geophysical Research: Solid Earth*, *122*(7), 5101-5117, doi:10.1002/2016JB013645.

Zimmerman, R. W. (2000), Coupling in poroelasticity and thermoelasticity, International Journal of Rock Mechanics and Mining Sciences, 37(1), 79-87, doi: 10.1016/S1365-1609(99)00094-5.